Modeling of Biofuelled HCCI Engines with a Parallel Multizone Model

by

Sona Visakhamoorthy

A thesis

presented to the University of Waterloo

in fulfillment of the

thesis requirement for the degree of

Master of Applied Science

in

Mechanical Engineering

Waterloo, Ontario, Canada, 2011

Declaration

I hereby declare that I am the sole author of this thesis. This is a true copy of the thesis, including any required final revisions, as accepted by my examiners.

I understand that my thesis may be made electronically available to the public.

Abstract

With growing concerns over emissions from various industries, homogeneous charge compression ignition (HCCI) engines offer a promising solution through reducing NO_x and particulate emissions and increasing efficiency. However, this technology is not without its challenges and numerical modeling of these engines can offer some insight into addressing these challenges. This study uses domain decomposition with FORTRAN MPI to subdivide computationally intensive sections of an existing 10 zone simulation model. Using an Intel i7 quadcore workstation the parallelized model reduced runtimes by half compared to serial computations. From here, two sets of biofuel experimental data were used to improve the validation base of the model. The fuels used were a simulated biomass derived gas (consisting of H_2, CH_4, CO, CO_2, and N_2) and a butanol/n-heptane blend. Once calibrated, the model showed good pressure, heat release, and products of incomplete combustion prediction for biogas. NO_x emissions were high, however the overall trend was captured. Similarly, once calibrated to the butanol/n-heptane data to account for some of the effects of negative valve overlap (NVO), excellent pressure and heat release predictions were obtained. However, products of incomplete combustion and NO_x were low and this was attributed to the inability of the model to properly account for inhomogeneity and all the effects of NVO. Once again though, the overall trend in NO_x levels was captured by the model. It was also found that the model does not operate very well near the misfire limit of the engine as it cannot capture the cyclic variability that can occur here. Based on the two new validation cases, it is concluded that once calibrated, the model can be used as a predictive tool for pressure, heat release, and combustion phasing of biofuelled HCCI engines. Furthermore, to improve its predictive capabilities, it is recommended that the model be restructured to incorporate mass transfer

between zones, a fixed crevice volume and variable thermal boundary layer, and a CFD solver to improve emissions predictions and reduce reliance on calibration. Finally, changing the zone distribution from ring like zones to lumped stirred reactors is recommended to allow for more realistic modeling of actual experimental HCCI conditions.

Acknowledgements

Over the course of this project, many people provided their support, help, insight, and feedback and I would like to take this opportunity to thank them. Firstly, I would like to thank my supervisor, Dr. John Wen, for offering me this position as a masters student on this project. The project was a very interesting change of pace from my usual interests and provided many new learning opportunities. Additionally, Dr. Wen was very accommodating and flexible and provided his time, support, and advice. One thing I appreciated was that he always maintained a "can do" attitude whenever I ran into any difficulties.

Next I would like to thank Tommy Tzanetakis from the University of Toronto, Mahdi Shahbakhti from the University of Alberta, and Dale Haggith from the University of Windsor for their knowledge and understanding of numerical modeling and experimental work involving various HCCI engines and fuels. They promptly provided very useful knowledge whenever necessary and gave feedback and advice on issues I may have overlooked. I would also like to thank Professor Andrezj Sobiesiak from the University of Windsor and Professor Charles Koch from the University of Alberta for allowing me to use their experimental data, without which much of this project would not have been possible. Finally, I would like to thank my lab mates, who were always open to discussion regarding topics from numerical modeling and experimental work to life in general and who helped in making my time here enjoyable.

Table of Contents

List of Figures

List of Tables

List of Acronyms

aBDC = after bottom dead center

bBDC = before bottom dead center

BDC = bottom dead center

BVP = butanol volume percentage

C_{BB} = blow-by constant

c_p = specific heat at constant pressure

c_v = specific heat at constant volume

CAD = crank angle degree

CFD = computational fluid dynamics

CH_4 = methane

CI = compression ignition

CO = carbon monoxide

CO_2 = carbon dioxide

DME = dimethyl ether

EGR = exhaust gas recirculation

EVO = exhaust valve open

H_2 = hydrogen

HCCI = homogeneous charge compression ignition

HRR = heat release rate

IVC = inlet valve closure

JSR = jet stirred reactor

K = number of species in chemical kinetic reaction mechanism

LCV = low calorific value

m = mass

MW = molecular weight

MPI = message passing interface

N_2 = nitrogen gas

NG = natural gas

NO_x = nitrogen oxides

NO_2 = nitrogen dioxide

N_2O = nitrous oxide

NTC = negative temperature coefficient

NVO = negative valve overlap

O_2 = oxygen gas

P = pressure

P_{cyl} = equalized cylinder pressure

PDF = probability density function

PRF = primary reference fuel

R_i = gas constant for zone i

R_l = ratio of connecting rod length to crank arm radius

R_u = universal gas constant

r_c = compression ratio

SI = spark ignition

SRM = stochastic reactor model

T = temperature

t = time

T_{in} = intake temperature (applied to core zone)

TDC = top dead center

u = specific internal energy

UHC = unburned hydrocarbons

V = zone volume

$V_{clearance}$ = cylinder clearance volume

V_{total} = total instantaneous cylinder volume

VVA = variable valve actuation

Y = species mass fraction

List of Symbols

β = blow-by parameter

γ = ratio of specific heats (c_p/c_v)

θ = crankshaft rotation angle

φ = air-fuel ratio

ρ = density

ω = engine speed

$\acute{\omega}$ = molar species formation rate

Chapter 1: Introduction

1.1 Motivation

With the ever increasing global population comes increases in energy use, agriculture, transportation use, and ultimately, greenhouse gas emissions [1]. The use of internal combustion engines in many of these industries can lead to increased amounts of emissions being released into the environment that can result in health problems and environmental damage. For example, unburned hydrocarbon (UHC) and nitrogen oxides (NO_x) are the precursors of photochemical smog which can cause health issues [2]. Particulate matter, such as soot, not only reduces overall air quality, but it can aggravate conditions for asthma sufferers [3]. To help address such increases, alternative engine technologies and fuels need to be considered. Homogeneous Charge Compression Ignition (HCCI) engines are one such technology that may help alleviate the environmental burden of increased transportation by offering reduced NO_x and soot emissions while operating at near diesel-engine efficiencies [4]. They offer a short to medium term solution to help bridge the gap from internal combustion engines to alternative technologies such as electric vehicles. HCCI engines can be considered as a hybrid between spark ignition (SI) engines and compression ignition (CI) engines where a premixed fuel is compressed until it is autoignited. These engines also offer the added benefit of being able to work with a wide range of fuels from low calorific value (LCV) fuels to natural gas, gasoline, and diesel [4] [5] [6] [7].

To further reduce environmental impact and reduce our dependence on petroleum, alternative fuels must also be considered. These alternative fuels can be in the form of gaseous biomass

derived fuels or liquid fuels. For example, the gasification of biomass can provide LCV fuels that have been successfully used in experimental HCCI engines [6]. Transesterification of oils derived from biomass such as soybean, canola, palm or microalgae can provide a source of renewable biodiesel and fermentation of sugar cane or corn can be a renewable source of ethanol. All of these fuels, when run in an HCCI engine, can provide an option for transportation that is cleaner and more environmentally friendly than current solutions.

In spite of the clear benefits of HCCI engines, there are some challenges associated with its implementation. The main challenge is that autoignition in HCCI is primarily driven by chemical kinetics and there are many factors that can influence it. This makes it inherently difficult to predict and control combustion timing and is a barrier to widespread commercial use. To address and better understand these factors, many engine models have been created. This thesis works with an HCCI engine model that was developed by a group from the University of Toronto [8]. The model was validated with two engine operating points using one set of experimental data which was for an engine running at 700 rpm using a primary reference fuel (PRF).

1.2 Objectives

Using the model developed by [8], the objectives of the current work consist of the following:

1. Improve the model such that computational times are reduced
2. Expand the limited validation base of the model using biofuelled HCCI experimental data

The validation of the improved simulation model will allow for the testing of the model's robustness and determine its limitations.

Chapter 2: Background and Literature Review

2.1 What is HCCI?

4-stroke HCCI engines are a promising extension [4] of current internal combustion engine technology in that they offer a design where SI-like emissions can be attained at CI-like thermal efficiencies. In HCCI a homogeneous air-fuel mixture is compression ignited with relatively large amounts of charge dilution. Unlike SI engines which are dependent upon a spark for combustion phasing and CI engines which depend upon fuel injection, HCCI combustion is completely controlled by chemical kinetics [4] and so depends on engine operating parameters such as temperature and pressure. For a brief comparison of HCCI to SI and CI, see Table 1.

Table 1: Comparison of key features between HCCI, SI, and CI engines

	HCCI	SI	CI
Homogeneous charge	Yes	Yes	No
Ignition	Compression	Spark	Compression
Ignition timing	Chemical kinetics	Spark	Fuel injection
High temperature flame	No	Yes - flame front	Yes - fuel rich regions

This autoignition of the premixed fuel-air mixture may lead to a large portion of the charge igniting nearly simultaneously and can be approximated as constant volume combustion [8]. However, the premixed air-fuel charge is never completely homogeneous, and there are subtle variations in temperature and concentration that can develop throughout the cylinder [9] [10]. This inhomogeneity varies from cycle to cycle and can occur due to variations in mixing and stratification caused by the relatively cool cylinder walls during compression, trapped residual gases, and in-cylinder turbulence [11]. Experimental work has shown that temperature

stratification in excess of 50K can occur between the core and the outermost layer of the charge during the compression stroke [9] [12]. Due to these effects and the dilute air-fuel mixture, a low temperature combustion event occurs with combustion occurring at different points throughout the cylinder [4] [7] [9] [13] and no discernible flame front [4] [14] [15] [16]. Even in well mixed homogeneous mixtures, this has been shown in optical engines, where different regions within the engine ignite simultaneously [9] [10] [11]. As each region ignites, it then compresses nearby surrounding gas thereby increasing its temperature and pressure. This leads to subsequent ignition of neighboring gas [9] [17]. The overall low temperature that occurs in HCCI combustion results in low NO_x levels and there is low soot and particulate formation due to a lack of fuel rich flame regions or localized high temperature regions which occur in diffusion flames present in CI engines. Furthermore, higher thermal efficiencies are possible due to the higher compression ratios required to autoignite such dilute air-fuel mixtures. Another benefit of HCCI engines is their ability to combust a wide range of fuels, similar to diesel engines. These fuels can range from low calorific value (LCV) fuels such as biomass derived gases (consisting primarily of CO and H_2) to natural gas (NG), alcohols, gasoline, and diesel [4] [5] [6] [7]. Furthermore, many of these fuels can be combined as blends such as n-butanol/n-heptane, ethanol/n-heptane, and n-butanol/gasoline [18] [19] [20].

These advantages along with HCCI engines' ability to combust a wide variety of fuels make it a very promising technology. However, this technology continues to have some inherent challenges associated with it. Some of these challenges have been overcome while others have been circumvented and allowed for HCCI engines to feature in prototype vehicles [21]. Production vehicles with HCCI engines are still some time away as there are still issues that must be met before widespread use of HCCI can occur. One of the main challenges of HCCI is

the fact that combustion phasing is completely controlled by chemical kinetics [4] and there is no specific ignition timing event as there is in SI and CI engines. For example, in SI engines, a spark times the combustion event, whereas in a CI engine, the timing of fuel injection is the trigger. Thus, HCCI is very sensitive to engine operating parameters.

Another challenge is the relatively high levels of UHC and CO emissions [4] [22] [23] [24]. These emissions generally have two main methods of formation. The first is where a significant amount of charge mass [4] is compressed into crevice regions of the engine during the compression stroke. In an SI or CI engine, this compressed gas escapes back into the cylinder during the expansion stroke and is oxidized by the high temperature of the exhaust gases present. However, in the case of HCCI engines, the exhaust gases present in the cylinder during the expansion stroke are the result of an already low temperature combustion event, and thus lack sufficient temperature to fully oxidize the released crevice region gases. This results in a significant source of UHCs and CO [25]. A secondary route of formation is via the thermal boundary layer that develops along in-cylinder surfaces of HCCI engines [17]. This boundary layer is on the order of one millimeter or less [9] [25] and gases here do not combust as a result of thermal quenching due to the relatively cooler in-cylinder surfaces. Additionally, as engine equivalence ratios are decreased to address lower load operating conditions, combustion temperatures correspondingly decrease thereby further increasing these emissions and reducing efficiency [4].

Dilute mixtures can also result in increased cyclic variability when operating near the misfire limit of the engine. This is due to the fact that in HCCI engines there can be a significant amount of charge dilution through EGR and trapped residual gases [26]. If a certain cycle lacks sufficient energy to completely combust, a significant portion of the unburned and partially

burned reactants is carried forward into the following cycle which then has improved combustion due to an effectively richer mixture. This is shown in Figure 1 [27] where a comparison is made between normal cyclic variation in peak in-cylinder pressure and misfired cyclic variation in peak pressure.

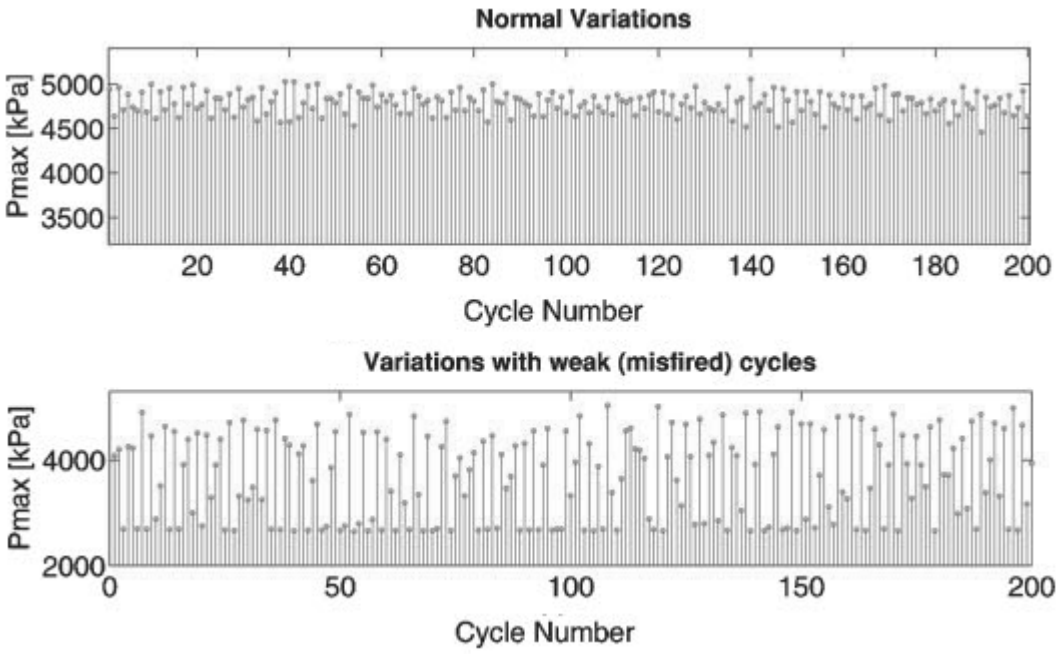

Figure 1: Comparison of cyclic variation in an HCCI engine [27]

Due to the increased emissions and misfire that occurs with dilute mixtures, these mixtures essentially define the low load limit of HCCI combustion [4]. Similarly, the high load limit of HCCI engines is limited by the rate of heat release during combustion [4]. As previously indicated, in HCCI a large amount of the charge gas ignites nearly simultaneously and at higher loads, the required richer fuel mixtures can lead to very high rates of heat and pressure rise. This can result in engine damage and high levels of engine noise. Due to this HCCI engines tend to have a narrow operating range which is a barrier to commercialization. Figure 2 [28]shows a HCCI engine's operating range compared to an SI engine operating range. From

this it is clear that the low load and high load limits need to be expanded to become commercially viable, or HCCI needs to be coupled with another mode such as SI.

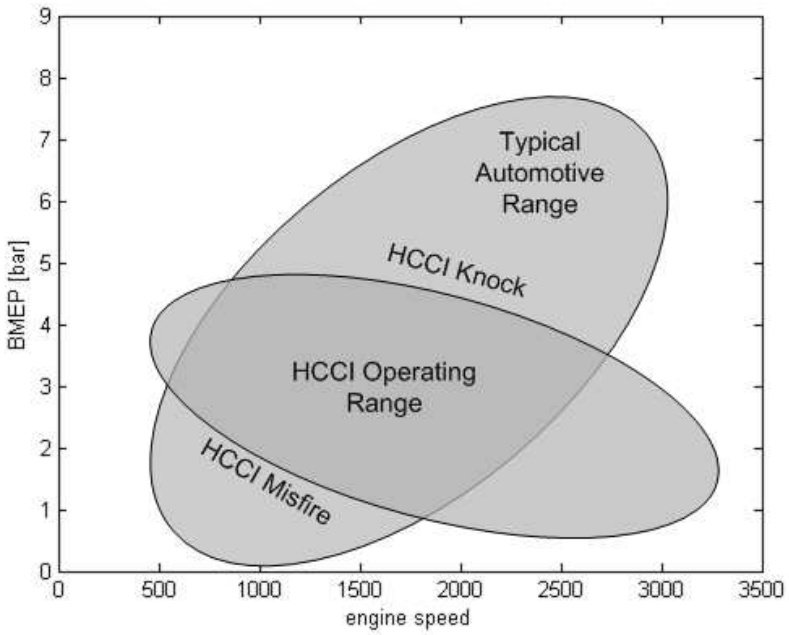

Figure 2: Comparison of HCCI operating range to that of a typical SI engine [28]

As previously mentioned, one method to expand the HCCI operating range is using engine mode switching. Other methods include using utilizing thermal and fuel stratification of the mixture to expand the operating range [29]. However, implementing engine mode switching has the added advantage of addressing another challenge of HCCI which is poor cold start behavior due to ignition depending on chemical kinetics. This occurs because of the very large thermal losses of the fuel-air mixture to the cold cylinder walls [4]. Starting the engine in SI mode and then switching to HCCI mode after it has warmed up can address this, however this has its inherent control and mixture preparation challenges.

2.2 Engine Control

To help alleviate some of the issues associated with HCCI combustion and to better control the combustion process, various engine control strategies have been implemented. These include varying the level of exhaust gas recirculation (EGR), adjusting equivalence ratio, changing intake temperature, varying compression ratio and implementing variable valve actuation (VVA). These methods can improve combustion stability, increase or decrease peak pressure behavior, advance or retard ignition timing, affect burn duration, and increase or decrease pressure rise rates.

The primary methods of controlling the combustion event dealt with in this report are through intake temperature, equivalence ratio, and VVA. Varying the intake temperature can advance or retard start of combustion and affect the heat release rate [30]. However, too high of an intake temperature will reduce overall efficiency as ignition will be advanced into the compression stroke. In experimental research HCCI engines, intake temperature is usually varied by preheating the intake air and then allowing the engine to warm up before taking any measurements [6] [26] [31]. However, in a practical engine, this can become difficult to directly implement as changes in temperature are transient and will take time to stabilize - nevertheless, it can be done indirectly through controlling trapped hot exhaust gases as this can be used to preheat subsequent engine cycles [30]. Similarly, adjusting equivalence ratio can be used to control heat release rates [30] in that richer mixtures result in higher heat release for higher loads. This method is limited by the high load limit of the engine. Finally, VVA can be used to improve ignition behavior of the engine. A specific form of VVA known as negative valve overlap (NVO) can be used where the exhaust valve is closed before all the exhaust has been completely evacuated from the cylinder, thereby trapping variable amounts of hot

combustion products [32] [33]. Typically, in SI engines, the exhaust valve is closed very near, or after TDC [32] to allow for the complete evacuation of exhaust gases. Closing the valve before TDC allows for a percentage of hot combustion products to remain trapped in the cylinder and be recycled into the subsequent engine cycle. The actual NVO period is the time during which both the inlet and exhaust valves are closed. This control strategy for HCCI allows for charge preheating by the trapped exhaust gases, causes thermal and compositional stratification to remain present up to ignition, promotes autoignition, and improves performance of the engine [11] [33] [34] [35]. HCCI engines can further benefit from NVO by timing part of the fuel injection within the NVO period (see Figure 3 [33]) which can allow for partial oxidation of the fuel prior to ignition. Varying the timing and quantity of the fuel injected during the NVO period can be used for low load combustion phasing control [35]. It can also improve combustion and expand the lower limit of the operating range [34] [35].

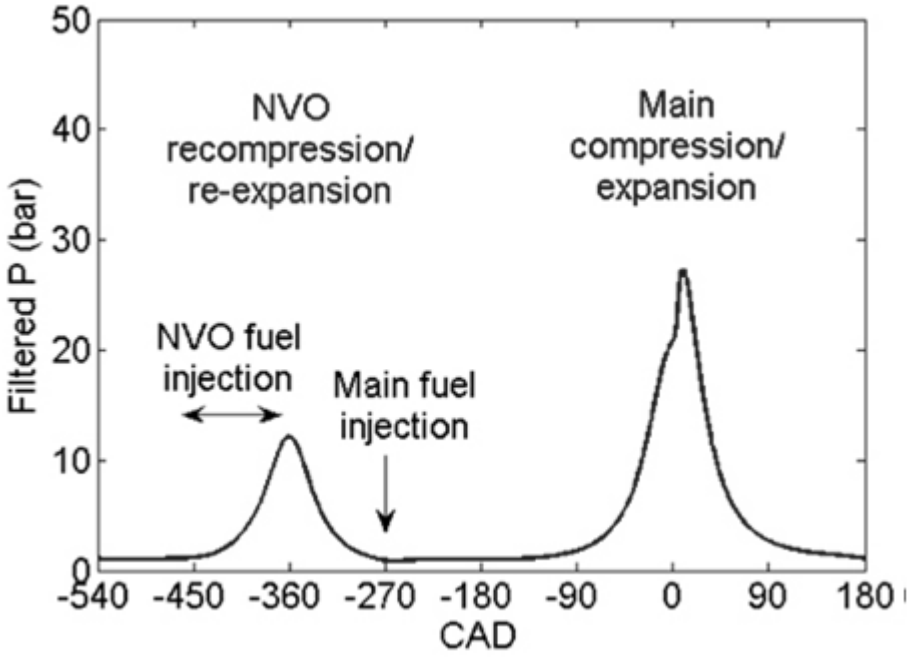

Figure 3: Pressure trace of a typical NVO equipped HCCI engine with NVO fuel injection [33]

In addition to the control methods discussed above, there are many others including varying EGR, utilizing fuel additives, fuel blends, adjusting compression ratio and others. For example, the concept of EGR is similar to NVO in that residual gases are recycled into the subsequent cycle. However, in the case of EGR, the trapped gases have cooled [30] since they have already exited the cylinder and passed through the EGR system. Thus their use is more as a charge diluent and they lower the reaction rate, thereby reducing peak pressures and heat release. Fuel additives can be used to stabilize HCCI combustion and extend a fuel's operating range. For example, combing DME with methane has been shown to improve the low load limit in HCCI combustion [30]. Similarly, blending fuels with different properties can also be used to modify the operating range in that neat fuels with differing autoignition characteristics will impact the autoignition behavior of the overall fuel. Finally, adjusting the compression ratio directly affects ignition timing and increased compression ratios will advance ignition. However, this is limited by the knock limit of the fuel and can be difficult to implement commercially.

2.3 Combustion Behavior of Paraffinic Hydrocarbon Fuels

Hydrocarbons form the basis of many fuels and understanding their combustion behavior is important to understanding certain trends in their heat release. These organic compounds only contain hydrogen and carbon atoms and are classified as either saturated or unsaturated. Saturated hydrocarbons, such as paraffins, consist of only single bonds between the carbon atoms in the molecule and are more stable than their unsaturated counterparts. Unsaturated hydrocarbons, such as olefins, are less stable and have double or triple bonded carbon atoms [34] [36].

One of the validation cases dealt with later in report deals with the combustion of a butanol/n-heptane fuel blend. N-heptane (C_7H_{16}) is a paraffinic fuel. Heavier paraffinic fuels (greater than 4 carbons) tend to exhibit two stage combustion under certain conditions. This combustion consists of three regimes: low temperature, intermediate temperature, and high temperature with a negative temperature coefficient (NTC) occurring at the end of low temperature heat release. Each of these regimes will be discussed in the following subsections.

2.3.1 Low Temperature Oxidation

Low temperature heat release occurs due to an initial rise in reaction rates caused by increasing temperature and follows reactions 1 to 7 shown below. The process begins with hydrogen abstraction by oxygen from the fuel creating various alkyl ($R\cdot$) and hydoperoxy ($HO_2\cdot$) radicals as shown by reaction 1.

$$RH + O_2 \rightarrow R\cdot + HO_2\cdot \quad (1)$$

The produced alkyl radicals are then consumed via two simultaneous pathways which become dominant in low temperature heat release: olefin production (reaction 2) and alkylperoxy radical production (reaction 3).

$$R\cdot + O_2 \rightarrow \text{olefin} + HO_2\cdot \quad (2)$$

$$R\cdot + O_2 \leftrightarrow RO_2\cdot \quad (3)$$

In reaction 2 olefins and hydoperoxy radicals are created by the abstraction of another hydrogen atom by oxygen. Reaction 3 shows the alternative pathway of alkyl radical consumption where an oxygen is added to the radical to create an alkylperoxy radical ($RO_2\cdot$).

The alkylperoxy radical is then internally isomerized through another hydrogen abstraction to create a hydroperoxyalkyl radical (·ROOH) as shown by reaction 4.

$$RO_2\cdot \rightarrow \cdot ROOH \quad (4)$$

Similar to earlier, the ·ROOH radical is consumed via two pathways which results in hydroxyl (OH·) radical production (reaction 5) and aldehyde (RCHO) and OH· radical production (reactions 6 and 7).

$$\cdot ROOH \rightarrow CARBONYL + R'\cdot + OH\cdot \quad (5)$$

$$\cdot ROOH + O_2 \leftrightarrow \cdot OOROOH \rightarrow HOOROOH \quad (6)$$

$$HOOROOH \rightarrow RCHO + R'O + OH\cdot + OH\cdot \quad (7)$$

Reaction 7 is essentially the end of the low temperature heat release, however, these equations alone do not describe why there is a decrease in heat release following the initial rise. At all temperatures, alkyl radical conversion to alkylperoxy radicals (reaction 3) is faster than olefin production (reaction 2). However, starting at approximately 700K at 10atm, the reverse alkylperoxy production reaction becomes dominant over the forward reaction thus increasing production of alkyl radicals [37]. These increased alkyl radicals are then consumed via the olefin pathway which leads to an increase in olefin production. This overall increase in olefin production reduces fuel consumption [37] leading to the decrease in heat release as temperatures increase seen in the later stages of the low temperature regime. The decrease in reaction rates is referred to as the negative temperature coefficient (NTC), or cool flame behavior.

2.3.2 Intermediate Temperature Oxidation

The intermediate temperature regime occurs after NTC and marks the beginning of increased reaction rates. As temperature is increased into this regime, olefin and hydoperoxy radical production continues to increase following reaction 2 of the low temperature regime. However, the increased level of hydoperoxy radicals results in increased production of hydrogen peroxide (H_2O_2) through abstraction of a hydrogen atom from the fuel as shown by reaction 8.

$$RH + HO_2\cdot \leftrightarrow R\cdot + H_2O_2 \quad (8)$$

As temperatures continue to rise, hydrogen abstraction continues creating an accumulation of hydrogen peroxide. The accumulated hydrogen peroxide then decomposes via reaction 9 creating two hydroxyl radicals for every hydrogen peroxide molecule. M represents any molecule that acts as a non-reactive collision base. The increased concentration of hydroxyl radicals results in an increase in reaction rates which marks the end of the intermediate temperature regime.

$$H_2O_2 + M \rightarrow OH\cdot + OH\cdot + M \quad (9)$$

2.3.3 High Temperature Oxidation

The radicals present at this point are very reactive and play an important part in the high temperature regime. Due to this, reactions in this regime proceed quickly beginning with reaction 10 and continuing to 13.

$$H\cdot + O_2 \rightarrow OH\cdot + O\cdot \quad (10)$$

$$O\cdot + H_2 \rightarrow OH\cdot + H\cdot \quad (11)$$

$$H_2O + O\cdot \rightarrow OH\cdot + OH\cdot \quad (12)$$

$$H\cdot + O_2 + M \rightarrow HO_2\cdot + M \quad (13)$$

Since the hydroxyl radicals react with hydrocarbons if available, once the hydrocarbons have been consumed, hydroxyl radicals begin to consume CO through reaction 14. The oxidation of CO to CO_2 represents a large fraction of the heat release, up to 50% [37]. Reactions 15 and 16 represent other forms of CO decomposition, however, the vast majority of CO is consumed via reaction 14 [37]. CO oxidation to CO_2 is an important aspect of combustion and incomplete oxidation results in loss of power which is one of the reasons for poor combustion efficiency of HCCI engines at low load conditions.

$$CO + OH\cdot \rightarrow CO_2 + H\cdot \quad (14)$$

$$CO + HO_2\cdot \rightarrow CO_2 + OH\cdot \quad (15)$$

$$CO + O\cdot + M \rightarrow CO_2 + M \quad (16)$$

2.4 Nitrogen Oxide Formation

One of the benefits of HCCI engines is their ability to reduce NO_x emissions due to the low temperature combustion that occurs within the cylinders. However, NO_x generation is still one of the major byproducts of the combustion process and an understanding of its major routes of formation can result in a better understanding of emission trends. There are five routes through which NO_x is produced [38]: thermal, prompt, fuel, NO_2, and N_2O.

2.4.1 Thermal

Also known as the Zel'dovich mechanism, the thermal route was discovered by Zel'dovich in 1946. In fuels with no fuel bound nitrogen, it becomes dominant at temperatures over 2500K

[38], however it becomes active at temperatures over approximately 1800K [3] [38]. The three core reactions to this mechanism are shown below:

$$O + N_2 \leftrightarrow NO + N \quad (17)$$

$$N + O_2 \leftrightarrow NO + O \quad (18)$$

$$N + OH \leftrightarrow NO + H \quad (19)$$

This mechanism exhibits an exponential dependence on temperature and requires temperatures in excess of 1800 to 1850K [3] [38] to proceed at an appreciable rate. This is due to the triple bond present in the molecular nitrogen of reaction 17 which has a high activation energy of 319kJ/kmol [38]. Reaction 17 is also rate limiting, and this in combination with its high activation energy result in the high temperature requirements. In addition to temperatures, increasing residence times increase the production of NO, however at equivalence ratios below 0.5, the effect becomes negligible [3].

2.4.2 Prompt

An important source of NO not described by the thermal mechanism was discovered by Fenimore. This route, known as the prompt mechanism, describes NO formation early in the flame when the thermal mechanism has not had time to fully establish itself. It is caused by hydrocarbon radicals reacting with molecular nitrogen forming hydrogen cyanide (HCN). HCN then reacts to create NO, through reactions 24-27. The main reactions which govern prompt NO formation are as follows:

$$CH + N_2 \leftrightarrow HCN + N \quad (20)$$

$$CH_2 + N_2 \leftrightarrow HCN + NH \quad (21)$$

$$CH_2 + N_2 \leftrightarrow H_2CN + N \quad (22)$$

$$C + N_2 \leftrightarrow CN + N \quad (23)$$

Reaction 20 is the primary reaction route and is rate limiting with an activation energy of 75-92kJ/kmol [38]. This is significantly less than the activation energy required for the thermal mechanism which explains how this mechanism can occur at much lower temperatures. Reactions 21 to 23 are minor sources of NO in the prompt mechanism as they have very high activation energies on the order of 300kJ/kmol.

$$HCN + O \leftrightarrow NCO + H \quad (24)$$

$$NCO + H \leftrightarrow NH + CO \quad (25)$$

$$NH + H \leftrightarrow N + H_2 \quad (26)$$

$$N + OH \leftrightarrow NO + H \quad (27)$$

2.4.3 Fuel

In certain fossil fuels, such as coal and its derivatives, nitrogen can be bound directly to the fuel. Some of this nitrogen can be converted to HCN and ammonia (NH_3). The reaction mechanisms of these two products leads to the production of NO. Somewhat increased NO levels can occur at increased flame temperatures since the amount of nitrogen that is converted from the fuel increases slowly with increasing temperature [3]. However, the NO formation from HCN and ammonia will not be discussed in detail as the fuels tested do not contain any nitrogen and the mechanisms are lengthy.

2.4.4 Nitrous Oxide (N_2O)

Another source of NO is a formation route through N_2O. N_2O is formed through reaction 28 and then consumed to become NO through reactions 29 to 31.

$$N_2 + O \leftrightarrow N_2O \quad (28)$$

$$N_2O + H \leftrightarrow NH + NO \quad (29)$$

$$N_2O + CO \leftrightarrow NCO + NO \quad (30)$$

$$N_2O + O \rightarrow NO + NO \quad (31)$$

2.4.5 NO_2

The final NO_x source introduced in this report is NO_2 formation. NO_2 formation occurs predominantly near the flame zone, and therefore, is likely a minimal source of NO_x emissions in HCCI engines as there is no discernible flame front. The governing reactions for this mechanism are outlined in reactions 32 to 34.

$$NO + HO_2 \leftrightarrow NO_2 + OH \quad (32)$$

$$NO_2 + H \leftrightarrow NO + OH \quad (33)$$

$$NO_2 + O \leftrightarrow NO + O_2 \quad (34)$$

2.5 Modeling Studies

To better describe the combustion process and design appropriate control strategies for HCCI engines, various simulation models have been developed that differ widely in terms of complexity and computational cost. The most commonly encountered models can be very broadly categorized into one of three groups: single zone models with chemical kinetics [39]

[40] [41], multizone models with chemical kinetics [17] [42] [43] [44] [45] [46], and CFD based models with chemical kinetics [47] [48]. However, to capture the statistical nature of certain aspects of combustion, another group of statistics based models called Stochastic Reactor Models (SRM) was introduced [49] [50] [51].

The simplest of the aforementioned models are the single zone models with chemical kinetics. Here the entire charge mass is treated as a single lumped zone of homogeneous temperature, pressure, and species concentration [4] [12]. Reaction rates and species evolution are solved using chemical kinetics. These models are easy to implement, have short computational times, and their main benefits are that they can give insight into ignition timing [4]. However, they tend to over predict heat release rates and pressure rise rates while under predicting certain emissions [4] [12]. This is due to the assumptions inherent to such models. For example, since the entire combustion chamber is treated as a single zone, these models lack any means of representing crevice regions and thermal boundary layers within the engine which are a significant source of CO and UHC emissions. Additionally, due to the single zone nature of the model, the entire gas mixture ignites at once without any staggered effect which leads to over prediction of heat release rate and NO_x [12].

To better differentiate between the bulk charge, thermal boundary layer, and crevice regions, multizone models were developed. Here, the in-cylinder charge is broken down into concentric ring-like [17] [25] [46] or individually lumped zones [35] [43]. Depending on the model, each zone is treated as a stirred reactor and is homogeneous in terms of species concentrations, temperature and pressure distributions, however, zones may be stratified against one another.

This can allow for the capture of species and temperature gradients throughout the cylinder. Depending on the model, mass transfer may also be implemented between zones [39] [44]. Once again, species evolution is solved using chemical kinetics. The advantage of these models is their ability to distinguish between cooler and hotter areas within the cylinder and account for localized generation of emissions. For example, the added resolution provided by thin zones along in-cylinder surfaces can help capture CO and UHC emissions due to thermal quenching. During the compression stroke, these models can account for mass flow into crevice regions, which can be over 35% of the charge mass [25]. Their ability to subdivide the cylinder into volumes also allows for thermal and concentration gradients to form which can further increase emissions and heat release rate prediction accuracy. However, depending on the number of zones and chemical mechanism being used, serial applications based on these models can become somewhat time consuming.

Both single and multizone models operate within the closed period of the engine cycle (between inlet valve closing (IVC) and exhaust valve opening (EVO)). Due to this, the initial conditions of the combustion chamber at IVC are user set parameters and are required inputs for the model. Many of these parameters, such as initial temperature stratification, the temperature of the charge once it has entered the cylinder, and blow-by losses are difficult to determine. Furthermore, the HCCI phenomenon is controlled by chemical kinetics and is very sensitive to changes in these parameters [8]. This can lead to inaccuracy within the model. To reduce this error and improve the inputs to the model, single zone models may have full engine cycle simulations added to run up to IVC at which point the numerical model takes over until EVO [52]. For example, linking a full cycle engine code such as GT-Power to a single zone

model will allow for a 1D representation of the working fluid which can then be used as an input for the model. However, since full cycle engine codes tend to be 1D, multizone models may be linked to a CFD solver such as KIVA which is used to determine initial gas mixing and temperature distribution prior to combustion [17] [42]. Once a certain piston position is reached, the multizone model takes over based on the temperature profile that was calculated by the CFD code.

Finally, there are pure CFD models where chemical kinetics is implemented along with CFD throughout the closed cycle period [47] [48]. Here mass and heat transfer can be solved along with any turbulence modeling of the compressed gases. Additionally, the intake stroke can be modeled for better overall predictive capabilities. CFD modeling can give good insight into specific engine features which promote turbulence such as the squish area of the pistons. However due to the level of detail involved and depending on the mesh size, these simulations can be very computationally intensive taking upwards of a month to run one simulation [4] [47]. Nevertheless, some work has been done to parallelize these models across computing clusters to reduce computational time [47].

Unlike the previously discussed models, the concept behind SRMs is that for a given set of initial conditions, the process of engine combustion is not a deterministic process with a fixed outcome. For example, for one stable engine operating point, all engine conditions remain the same, however there can be cycle to cycle variation in peak pressure. To address this random aspect of combustion, HCCI SRMs can replace the assumption of homogeneity with that of statistical homogeneity to capture subtle inhomogeneities in the mixture [49] [50] [53]. Here

physical properties of the mixture such as mass, temperature and species concentration are described by probably density functions (PDFs). These PDFs are time dependent and will change depending on the crank angle. Similar to single zone models, SRMs can also be linked to a full cycle engine simulation code such as GT-Power for a comprehensive modeling package [50] [54] [55] [56].

2.6 Numerical Model

For this study a 10 zone multizone model [8] with chemical kinetics was used to numerically solve the species evolution, temperature, and pressure within the cylinder. It operates during the closed cycle period of the engine between IVC and EVO. It has been reported [8] [12] [44] that 10 zones is sufficient for solving in-cylinder pressure traces although the selection of the number of zones is flexible for parallel computing. This model steps through species, temperature, and pressure evolution for each incremental crank angle of one engine cycle. It considers heat transfer between zones and the cylinder walls, but does not consider mass transfer. There is, however, mass loss due to blow-by and this is implemented by an equivalent loss of mass from all zones. Heat transfer coefficients are determined using the Woschni correlation which accounts for bulk gas velocity caused by piston movement.

Since the model begins operation at IVC, initial conditions are difficult to determine. Exact experimental values for many of the required input parameters are generally unknown or difficult to determine from the experiment which is why they need to be calibrated. For example, the intake temperature of the overall charge at IVC will not be the measured temperature in the intake manifold due wall heating of the charge, pre-heating caused by trapped hot residual gases, and vaporization of injected fuel [46]. To calibrate the model to a

given set of experimental data, there are a set of adjustable parameters. Once a suitable set of calibrated parameters has been determined for a single engine operating point, these parameters are left unchanged when the model is used as a predictive tool for other operating points. However, differences between calibrated parameters and their actual experimental values can lead to sources of error in the model. Table 2 shows a list of the adjustable parameters and a brief description of each one.

Table 2: Description of adjustable model parameters

Parameter	Description
cbb	Blow-by constant
corepct	Fraction of cylinder volume allocated to the core zone
geomr	Geometric ratio - how rapidly zones get thinner as they approach the wall
tintake	Intake temperature of the air fuel mixture
htcfac	Heat transfer scaling factor applied in Woschni correlation
twidth	Temperature difference between the outermost and core zones
resfrac	Fraction of trapped residual gases
twall	Cylinder wall temperature - assumed to remain spatially and temporally constant

2.6.1 Algorithm

As previously indicated, the numerical model solves species evolution, temperature, and pressure within the cylinder from IVC to EVO. To do so, the model follows the algorithm outlined in the flow chart in Figure 4 [8].

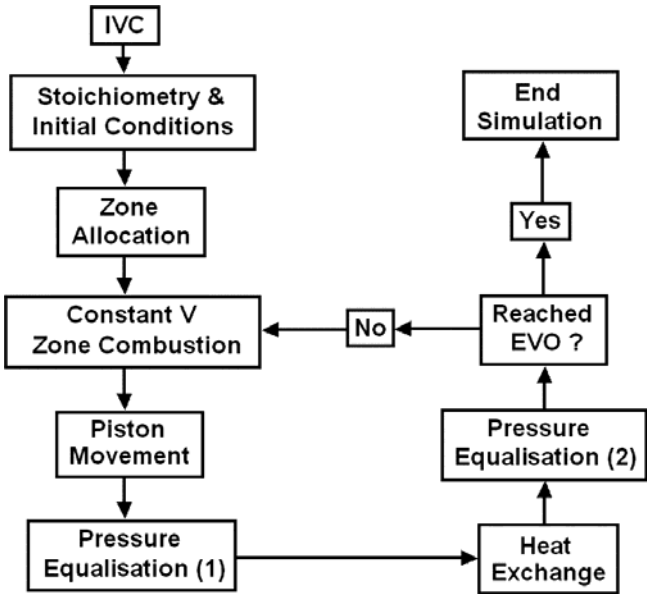

Figure 4: Flow chart of numerical algorithm [8]

Following IVC, the model divides the cylinder into a cylindrical core zone with successively larger ring-like zones surrounding it as shown in Figure 5. Zones can be of equal thickness or specified to become successively thinner as they approach the cylinder wall. Crevice zones were not specifically included in the model, however they can be lumped into the single outermost zone. Each zone is homogeneous in terms of temperature, pressure, and species concentration; however, these values can stratify amongst zones. Neighboring zones only interact via moving boundary work and heat transfer - there is no mass transfer considered in this model though there is mass loss due to blow-by. As briefly indicated earlier, since there is no mass transfer between zones, blow-by losses are applied equally to all zones.

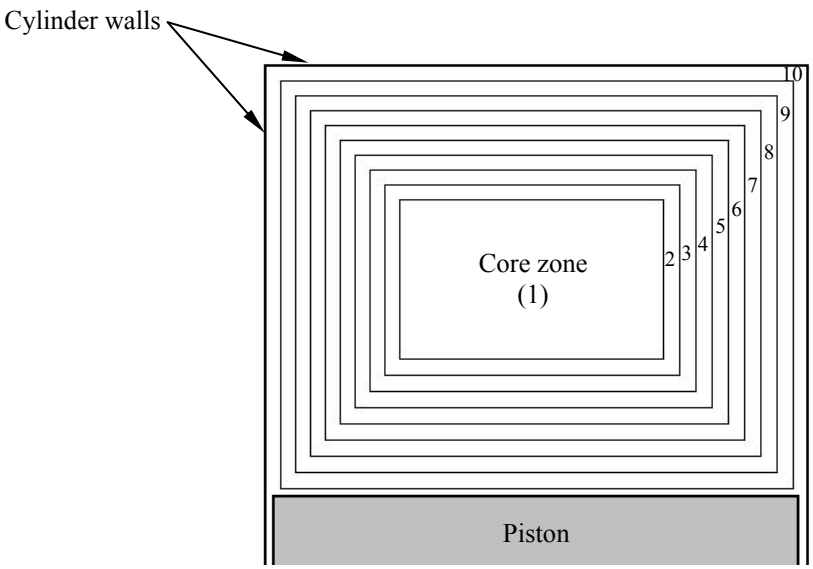

Figure 5: Breakdown of cylinder into individual zones

Once the zone dimensions are specified each zone sequentially undergoes constant volume combustion. Here, the species and energy conservation equations (Equations 35 and 36) [8] are solved using thermodynamic properties and reaction rates from Chemkin. Each zone is solved independently of the others and the outcome of any zone has no effect on any other zone *at this point* - thus the zone states can be solved in any order. After species evolution is complete zone temperature, volume, and molar quantities are known and individual zone pressures can be calculated using the ideal gas law (Equation 37) [8].

$$\frac{dT}{dt} = -\frac{1}{\rho c_v}\sum_{j=1}^{K} u_j \dot{\omega}_j MW_j) \tag{35}$$

$$\frac{dY_j}{dt} = \frac{\dot{\omega}_j MW_j}{\rho} \tag{36}$$

$$P = \frac{\rho R_u T}{MW_{mix}} \tag{37}$$

Immediately following constant volume zone combustion, zone temperature, pressure and species concentrations are known. However, during combustion the piston is also moving. To account for this, the overall cylinder volume changes according to Equation 38 [36].

$$\frac{V_{cylinder}}{V_{clearance}} = 1 + \frac{1}{2}(r_c - 1)(R + 1 - cos\theta - \sqrt{R^2 - sin^2\theta}) \quad (38)$$

Following this volume change, a pressure equalization step is carried out which accounts for any heat release during constant volume zone combustion and piston movement (overall system volume change). This first equalization step also accounts for blow-by losses from each zone. Zones that had previously increased in temperature due to heat release now have the opportunity to expand against lower temperature zones thereby increasing their volume. The pressure throughout the cylinder is assumed to equalize instantly. Using this assumption and the newly established cylinder volume along with Equations 39 and 40 [8]the final thermodynamic state of each zone can be determined.

$$P_{cyl} = \frac{\sum_{i=1}^{N_{zones}} m_i^o c_{v,i}^o T_i^o \left(\frac{1}{\gamma_i^o - 1} - \frac{1}{\beta}\right)^{-1}}{V_{total} - \sum_{i=1}^{N_{zones}} V_i^o \left(\frac{1}{\gamma_i^o - 1} - \frac{1}{\beta}\right)^{-1}} \quad (39)$$

$$V_i = \left(\frac{m_i^o c_{v,i}^o T_i^o \beta + P_{cyl} V_i^o}{P_{cyl}}\right)\left(\frac{1}{\gamma_i^o - 1} - \frac{1}{\beta}\right)^{-1} \quad (40)$$

At the end of this phase each zone has unique volume, species concentration, and temperature though equal pressure. This allows for heat transfer to occur between zones and between the outermost zone and the cylinder walls. Heat transfer in HCCI engines is thought to be primarily driven by forced convection with minimal radiation effects [57]. The improved

Woschni correlation (Equation 41) [58] is used to calculate the heat transfer coefficient between the gas and in-cylinder surfaces. However, in HCCI engines, turbulence is evenly distributed throughout the cylinder and thus, the heat transfer is as well [8]. Therefore, the heat transfer coefficient calculated by the Woschni correlation is then treated as an overall heat transfer coefficient and applied between all zones and the outermost zone and the wall. The Woschni correlation is based on instantaneous cylinder height, temperature, and pressure while also containing a term which accounts for bulk gas velocity.

$$h(t) = \alpha_{scaling} L(t)^{-0.2} P(t)^{0.8} T(t)^{-0.73} v(t)^{0.8} \quad (41)$$

After heat transfer, zone pressures and temperatures will have changed due to energy loss or gain. Another pressure equalization step is performed after which the thermodynamic state of each zone is known. For a pictorial illustration of the overall numerical algorithm, see Appendix D.

Chapter 3: Model Development – Programming

3.1 Minor Improvements

The numerical model used in this study was originally developed as a 32 bit serial application written in FORTRAN 77. However, some minor improvements were made to the model before parallelizing it to reduce computation time.

When running at a resolution of 0.0042 CAD the model took approximately 15 minutes to solve a 10 zone system using the reduced PRF mechanism of 32 species and 55 reactions from [59] which was the original calibration system used in [8]. Updating the model to work in a 64 bit environment and compiling it as a 64 bit application reduced runtime for the same initial system by nearly 2 minutes. This reduction in runtime is attributed to the fact that 64 bit processing allows for double the bandwidth of 32 bit processing. Another benefit of a 64 bit application is that it will have access to more RAM than a 32 bit application if necessary. Other improvements included updating the majority of the code to FORTRAN 90 to improve legibility, and setting many of the input parameters as values in an initial input file as opposed to having the values hard coded into the program which requires the program to be re-compiled every time a parameter is changed.

3.2 Parallel Processing

To further reduce runtime and possibly improve spatial resolution by running more zones, the serial code was parallelized using Message Passing Interface (MPI) for FORTRAN. The premise of parallelizing the simulation was to share the most computationally intensive step across multiple processes. To determine which phase of the numerical algorithm was most computationally intensive, the code was run using the initial validation case from [8] but at a

coarse timestep (resulting in a CAD resolution of 0.042) to reduce runtimes to less than 2 minutes. Using the original calibrated parameters 5 runs were conducted. From here, each main phase of the numerical algorithm was timed, and the overall breakdown of time spent in each area is shown in Table 3 with the average time spent shown in Figure 6.

Table 3: Breakdown of time spent in each area of the model for 5 runs

Total CPU Time (sec)	**Region 1 (sec)**	**Region 2 (sec)**	**Region 3 (sec)**	**Region 4 (sec)**
82.8	$1.56x10^{-2}$	78	0	1.28
82.8	$1.56x10^{-2}$	78.3	0	1.06
82.8	$1.56x10^{-2}$	78	0	1.00
82.8	$1.56x10^{-2}$	78	0	1.17
82.8	$1.56x10^{-2}$	78.2	0	1.19
Total CPU Time (sec)	**Region 5 (sec)**	**Region 6 (sec)**	**Region 7 (sec)**	**Region 8 (sec)**
82.8	2.63	0	1.09	$3.13x10^{-2}$
82.8	3.11	0	1.33	$1.56x10^{-2}$
82.8	3.03	0	0.922	0
82.8	2.83	0	1.14	0
82.8	2.78	0	1.06	0

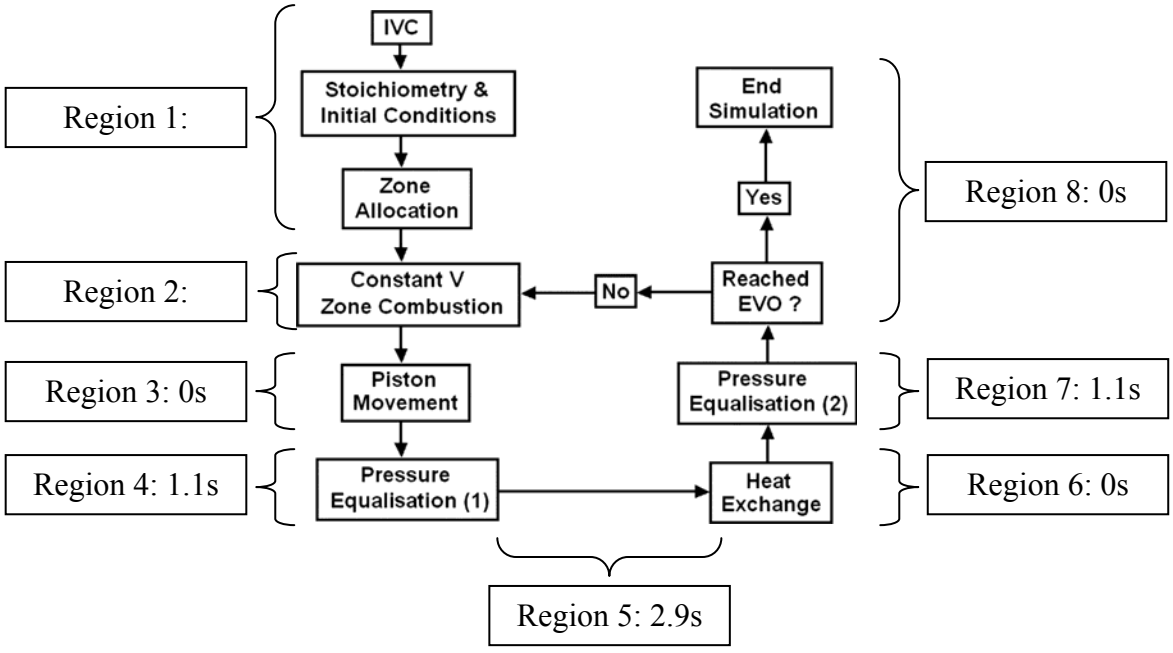

Figure 6: Average time spent in each area of the model

From the data, it is clear that constant volume zone combustion is the most time consuming step (using 94% of computational time with a 32 species/55 reaction mechanism). Furthermore, this step was also identified as consuming, proportionally, increasing amounts of simulation time as the complexity of the chemical mechanism was increased.

The constant volume combustion step is solved sequentially for each of the ten zones. In an ideal case, the individual combustion step for each zone would be parallelized, but this was impossible due to data dependence within the algorithm. However, the next best option was to implement domain decomposition and split the domain across multiple processes for parallelization. Since each zone in the model effectively represents a subdomain of the overall data domain, this method lends itself very well in this situation. A flowchart (a modified version of the one found in [8]) for the parallel simulation is presented in Figure 7. Each zone (or a few consecutive zones) can then be passed to a different process to be solved in parallel. As indicated earlier, the sequence in which the zones are solved during constant volume zone combustion is irrelevant as the evolution of species and thermodynamic properties within each zone is completely independent of other zones during this step. Therefore, there is no data dependence between zones and parallelization of this step is possible using domain decomposition.

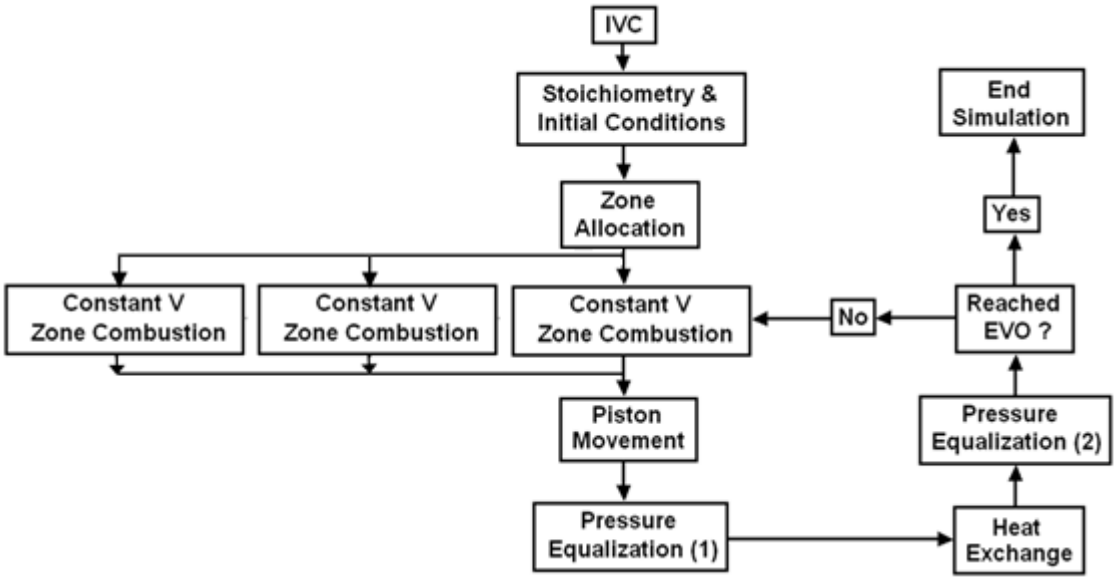

Figure 7: Flow chart of parallelized algorithm

In an ideal case of parallelizing, Amdahl's law [60] can be used to predict the maximum speed up that can be expected based on the number of processes across which the code is parallelized and the percentage of code that can be parallelized as shown in Equation 42.

$$Speed\ Up = \frac{1}{(1-P)+\frac{P}{N}} \tag{42}$$

Assuming that 94% of the code is parallelized, the potential speed up gained is shown in Figure 8. As it can be seen, increasing the number of processes past 50 quickly results in diminishing returns due to the small fraction of serial code [61]. However, since the data is broken down by zones, the current 10 zone model can, at most, be parallelized across 10 processes since further decomposition is not possible. After this, improvements would come from simplifying the reaction kinetics or increasing the processing power of the individual processors across which the model is parallelized. However, if the number of zones were increased, then further speed ups are quite possible.

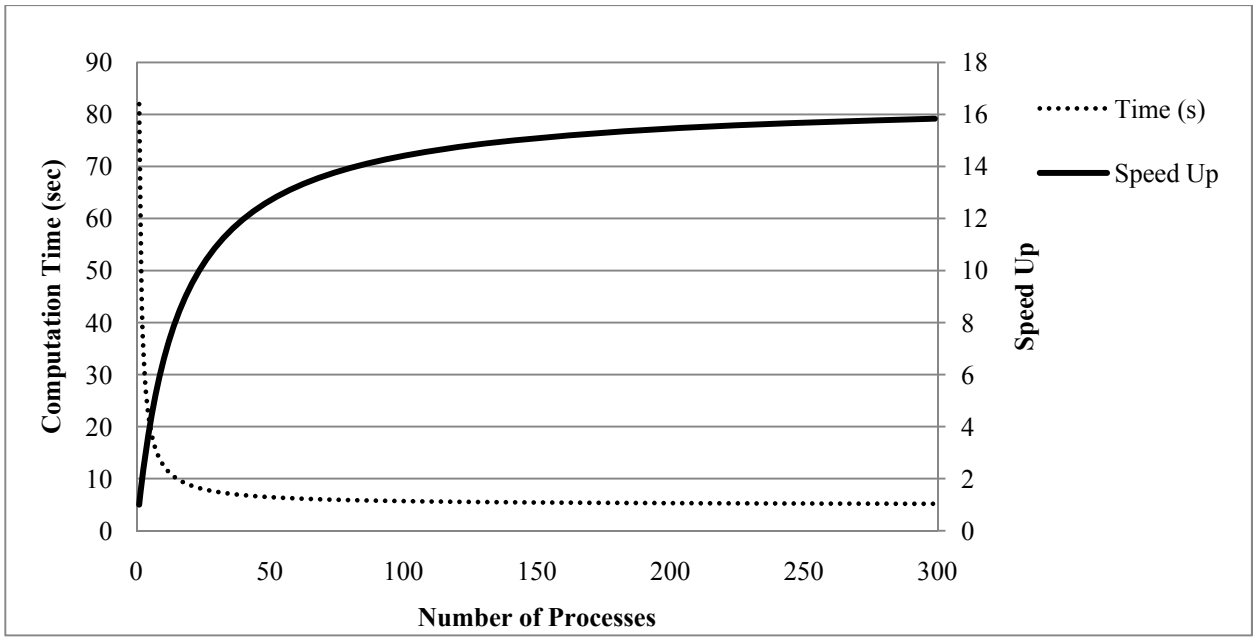

Figure 8: Ideal speed up based on number of processes

An interesting corollary to this is that as the complexity of the chemical mechanism is increased, gains through parallelization should increase for a given number of processes. This is due to the fact that larger mechanisms result in an increased proportion of computational time being spent in the constant volume zone combustion step. However, this does not necessarily occur due to the fact that larger mechanisms also consume more memory and CPU time through the arrays required.

It should be noted though, that Amdahl's law is a purely ideal case and that in practice, the improvements in the code will not achieve the predictions. This is due to inefficiencies in the code and computational overhead incurred due to parallelization. For example, running this simulation with the calibration case from [8] as a 10 zone model at a resolution of 0.0042CAD across a quad core workstation results in a speed up of almost 1.9 (reduced another 5 minutes of computational time to around 8 minutes) where Amdahl's law predicts a speed up of 3.4.

The difference here is likely due to the fact that with MPI there is considerable inter-process communication occurring as large arrays (or sections of arrays) are sent back and forth between processes. This inter-process communication can become significant as chemical mechanisms become more complex and this will incur losses in computational efficiency.

3.3 Results

Using the parallelized numerical simulation, two sets of validation cases were conducted and will be discussed later in this report. However, the runtime results from both sets exhibited adequate gains as shown in Figure 9. The two new validation cases are presented along with the previous validation case from [8]. All three cases in the comparison were completed using the same temporal resolution to allow for proper comparison and were run on a quadcore Intel i7 processor in both serial and parallel mode. A speed up of 1.9 was gained for the original validation data (55 reactions, 32 species), however speed ups in excess of 2 were gained for the newer validation cases. In the case of the biogas work, a speed up of nearly 2.4 was achieved at a mechanism size of 771 reactions and 135 species. For the butanol/n-heptane validation work, a speed up of 2.1 was achieved with a mechanism size of 1805 reactions and 200 species.

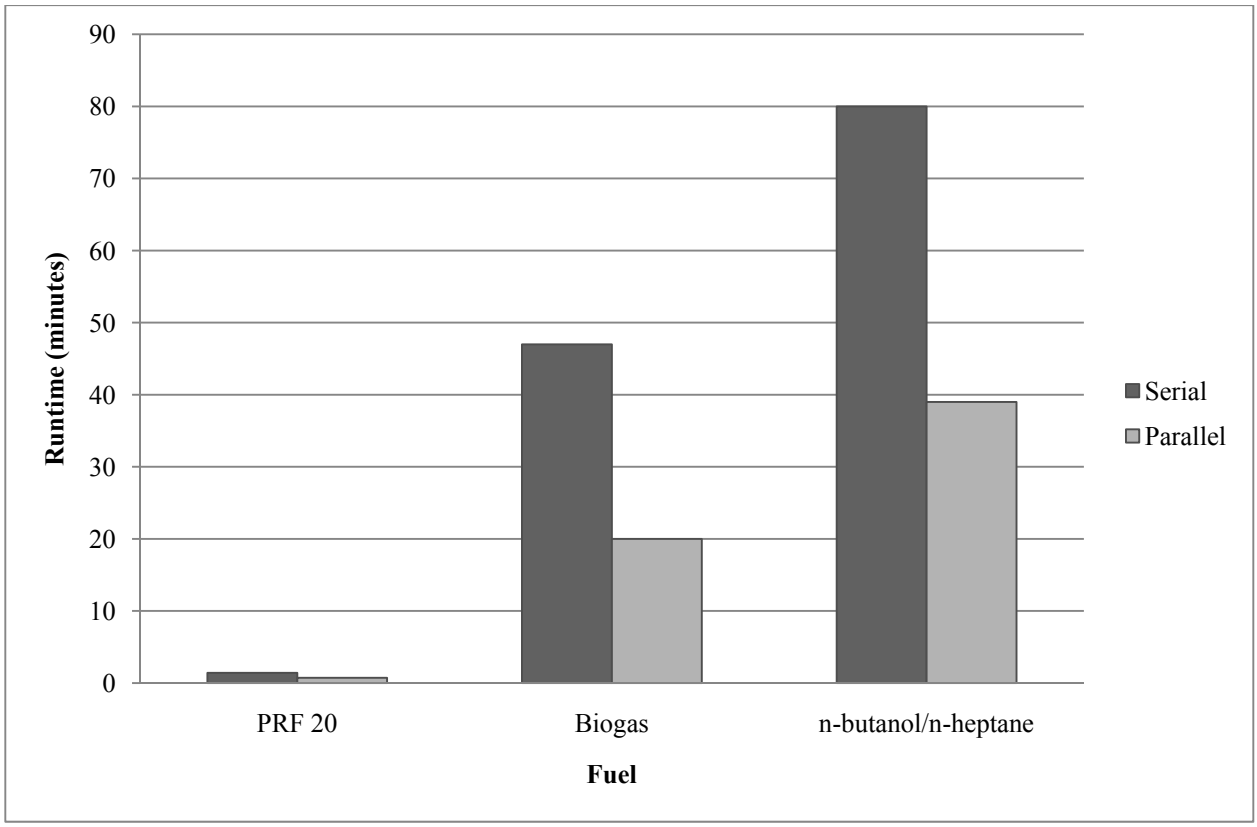

Figure 9: Comparison of serial and parallel computation times for different validation cases

With the benefit of a parallelized model, some work was then conducted to determine whether increasing the number of zones was a feasible way to increase the accuracy of the model. However, it was found that changing the number of zones essentially changed the overall system being solved which would require the model to be recalibrated.

When the number of zones was increased for the original validation data of the model, it was found that the total mass of the charge present within the cylinder immediately after IVC increased slowly. The trend is shown below in Figure 10.

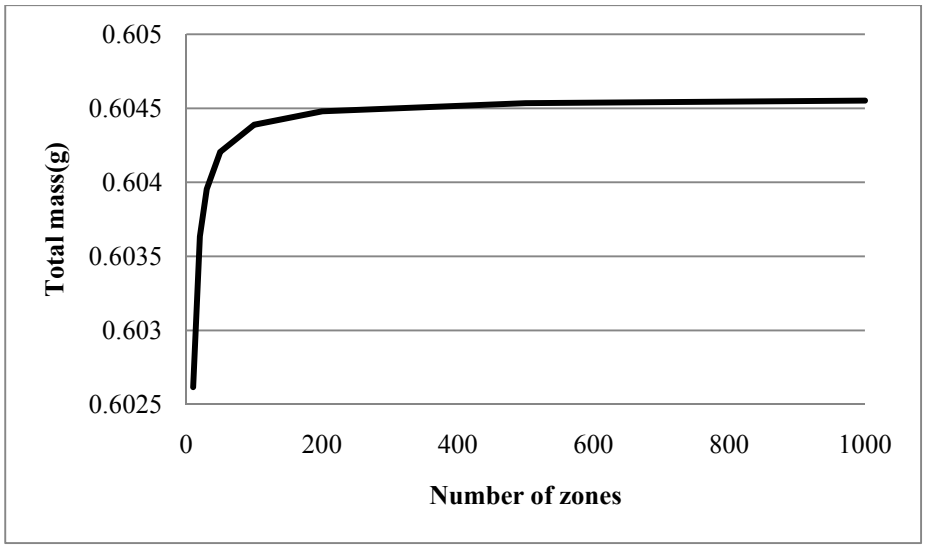

Figure 10: Total charge mass vs. number of zones

As it can be seen from this trend, the overall charge mass increases as the number of zones is increased, however it does show a rapid decrease in the size of the increase. This would indicate that the combustion system changes when the number of zones is changed. The change in mass is caused by temperature stratification of the initial charge. During the initial mass allocation section of the numerical algorithm, mass within each zone is calculated based on the number of moles and the molar mass of the mixture. However, the number of moles in each zone will vary as indicated by the ideal gas law. At IVC, all zones have the same pressure, and any changes in temperature will cause variation in the number of moles. Therefore, since the initial volume of the model is fixed and the temperature stratification is set by the user, the overall gas mixture mass will vary due to variations in the density as the number of zones is changed. This occurs because different regions of the cylinder will have different bulk temperatures and therefore different masses as calculated by the ideal gas law. Figure 11 below clarifies an example case.

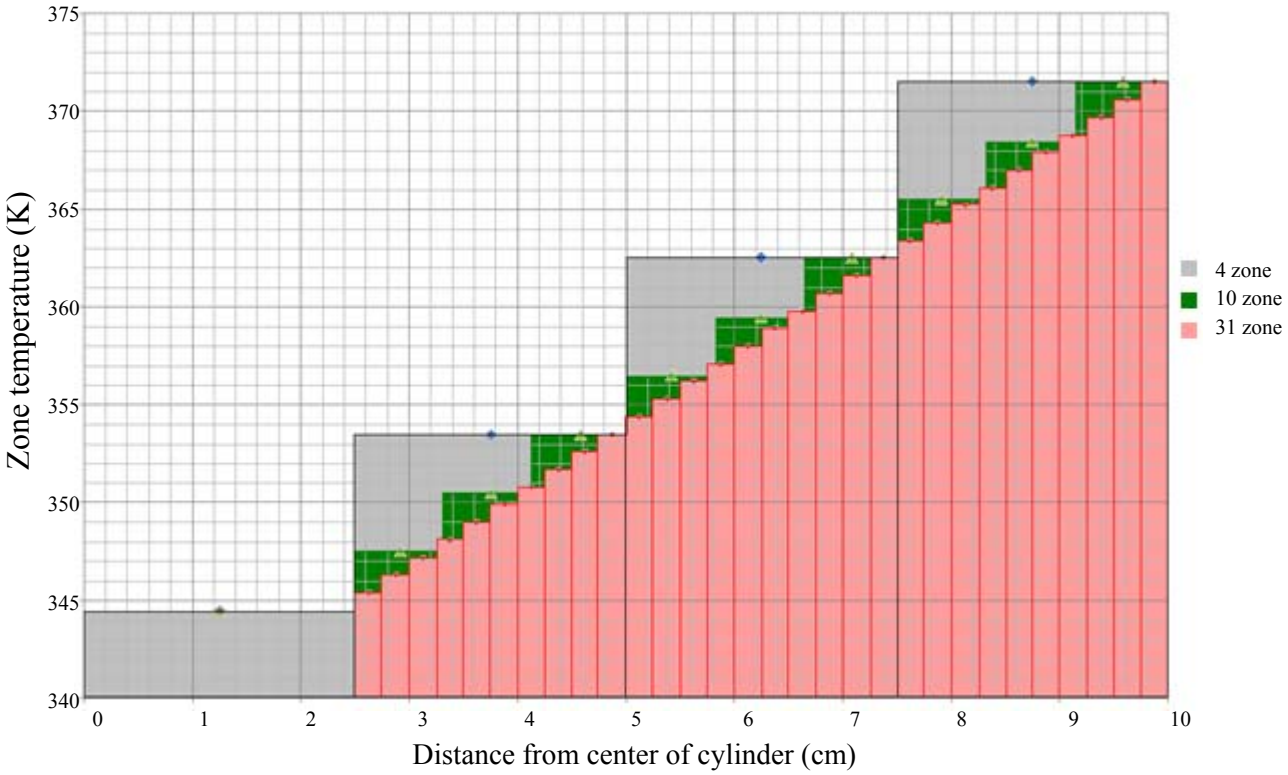

Figure 11: Changes in temperature distribution due to spatial resolution

Since the volume of the core zone remains fixed, increasing the number of zones further subdivides the region outside of the core zone. Thus, if a positive temperature gradient is held constant, the mean temperature for a given fixed zone size decreases. This decrease in temperature results in a higher mean density for a given volume, and therefore, more mass for the total charge. In the example above, the model is set to have a core zone temperature of 344.5K and a thermal width of 30K to the outermost zone. If one looks at the 4 zone model (gray), it can be seen that the outermost zone has a thickness of 2.5cm and a constant temperature of 371.5K. Now, consider the outermost 10 zones of the 31 zone model (red). These 10 zones occupy the exact same volume that the single outermost zone of the 4 zone model did. However, in the case of the 31 zone model, only the outermost zone with a thickness of 0.25cm is at 271.5K. The other 9 outside zones are at progressively cooler temperatures and so have progressively higher densities. As mentioned earlier, the numerical

algorithm calculates the mass of each zone based on the number of moles which changes due to density. Due to this, the model calculates a higher mass for a given volume of the cylinder since the bulk gas temperature becomes cooler as the number of zones is increased. This effect is further corroborated by the fact that for a fixed set of inputs, increasing the number of zones caused increasing peak pressures with a trend very similar to that shown by the increasing mass, as shown in Figure 12. Once again, peak pressures rose fairly quickly initially and then leveled off in the later stages. The peak pressure increase is caused by the increased amount of charge available for combustion.

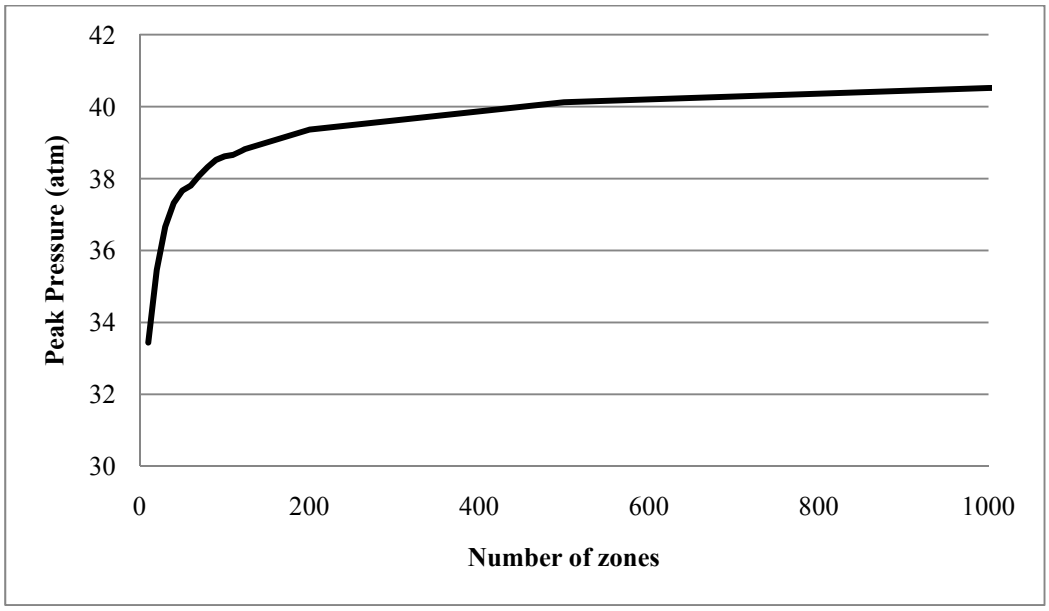

Figure 12: Peak pressure behavior as the number of zones is increased for a fixed set of initial conditions

This effect can also be observed if the core zone is the hottest and there is a negative temperature profile towards the outermost zone. So it can be concluded that running more zones in the model does paint a more accurate picture of the thermal stratification, however it does change the overall system and requires recalibration of the model which can be a lengthy process. Since the system changes tend to stabilize after approximately 200 zones, it is possible

that calibrating the model to this point would be more accurate than the 10 zone model and would not require any further increases in the number of zones. However, such a large number of zones is not necessary for the purpose of this report and is also very time consuming to run. Due to this, for the purpose of analyzing pressure and heat release trends as in the case of this study, a 10 zone model is sufficient [8] [44].

Chapter 4: Biogas Validation

4.1 Biogas

As indicated previously, a major benefit of HCCI engines is their ability to combust a wide range of fuels from LCV fuels to heavier fuels such as diesel. Running LCV green fuels such as biomass derived gas has long been done in conventional SI and CI engines [62]. However, testing of these fuels in HCCI engines has not been widely studied, though some experimental work has been done to show that it is a viable option [6] [7].

Biomass derived gas, also known as producer or wood gas, is derived from the gasification of biomass or bio-residues [62]. Depending on the source, processing conditions and method, biomass gas contains varying amounts of methane, carbon dioxide, carbon monoxide, hydrogen, nitrogen, and water vapor [6]. The gas analyzed in this study is a simulated biomass gas designed to mimic producer gas' composition of low levels of CH_4, relatively high levels of CO, H_2 and CO_2, and high levels of N_2. Water vapor is omitted as the gas is assumed to be dry [6]. The significant difference between biomass derived gas and NG and syngas is the very low CH_4 content. Thus, the majority of energy release is derived through the combustion of H_2 and CO. Additionally, the high levels of CO_2 and N_2 act as knock suppressors tending to give this fuel a relatively high octane rating [62] making it more suitable for high compression ratio applications. Further benefits of using a biomass derived gas in HCCI combustion include it being a renewable fuel and lower NO_x emissions due to it having no fuel bound nitrogen. A misconception that is sometimes associated with LCV fuels is that due to their very low energy content per unit of fuel, there is a significant de-rating of engine power when compared to more conventional NG or gasoline fuelled engines. Producer gas' calorific value is

approximately 6.8MJ/kg [63] whereas NG is around 45MJ/kg [64] and ethanol is approximately 27MJ/kg [65] [64]. The calorific values of the mixtures used in the experimental work being modeled are 4.27 and 4.41MJ/kg [6]. Thus it is fairly clear that LCV fuels have significantly less energy per unit mass. However, when comparing these fuels on a per unit mixture basis, the difference in energy content becomes less due to the charge dilution that is required in internal combustion engines. In the case of HCCI engines, the amount of charge dilution can become significant (on the order of φ=0.4) and so the energy content of the overall mixture becomes closer to that of higher calorific value fuels. Thus there is not a significant de-rating of power due to the use of LCV fuels.

4.2 Reaction Kinetics

The main compounds which contribute to combustion in the simulated biomass gas are H_2, CO, and CH_4. These compounds have been fairly well studied at relatively low pressures and there are many chemical mechanisms which model their behavior such as the PRF model, Konnov 0.5, Marinov, Gri-Mech 3.0, Leeds, RAMEC, and Petersen et. al. However, not many of these are best suited for simulation of a biomass gas fuelled HCCI engine. Experimental results of these engines indicate peak pressures in excess of 80 atmospheres [5] [6]. Furthermore, work by Petersen et al. [66] indicates that the $CH_3O_2 + CH_3 \rightarrow CH_3O + CH_3O$ reaction is important for CH_4 combustion at pressures over 10 atmospheres [67] [68] [69] and this reaction pathway is not present in some of the more widely used models.

The GRI-Mech 3.0 [70] mechanism has a wide experimental base and has been validated to approximately 10 atmospheres [67] [68]. It includes a NO_x mechanism, however, it does not include the CH_3O_2 pathway. Similarly, the Leeds [71] [72] mechanism has an equally wide experimental base but also does not include the CH_3O_2 pathway. The Konnov 0.5 [73]

mechanism does not have nearly as extensive an experimental base as GRI-Mech 3.0 though it has been validated at relatively low pressures and includes the CH_3O_2 pathway. Additionally, the majority of the Konnov mechanism's validating experiments do not focus on the hydrocarbon compounds [67]. In light of the deficiencies in these widely used mechanisms, Petersen et al proposed the RAMEC [66] model for high pressure low to mid-temperature CH_4 oxidation. This model includes the CH_3O_2 pathway however its experimental base is somewhat limited to only shock tube data. To further improve this model and apply it to a wider range of conditions, Petersen et al introduced a new model with 118 species and 663 reactions. This model also includes the CH_3O_2 pathway but is validated against different shock tubes and jet stirred reactors (JSR). Neither the RAMEC or Petersen et al mechanisms include NO_x mechanisms and neither of them are as extensively validated as GRI-Mech 3.0, Leeds, or Konnov.

Various papers [74] [75] [76] have shown that GRI-Mech 3.0, PRF, Konnov and RAMEC capture the general trend of ignition delays but tend to over predict or under predict the results. They do, however, fall within the experimental error of the data. Interestingly enough, both GRI-Mech 3.0 and Konnov mechanisms show similar trends (GRI over predicts, Konnov under predicts) even though Konnov has the CH_3O_2 pathway. At higher pressures approaching 150atm, GRI-Mech 3.0 and Konnov 0.5 continue to predict similar trends in CH_4/O_2 combustion [77]. The RAMEC mechanism shows good agreement with some experimental data compared to the GRI-Mech 3.0 mechanism, however, the newer Petersen et al mechanism shows better predictions over a wider data range. [78] showed that the new Petersen et al mechanism has excellent results (compared to GRI-Mech 3.0, RAMEC, and Leeds) for the

combustion of pure hydrogen, methane, and hydrogen-methane mixtures in a rapid compression machine at pressures up to 70 atm.

For this study, the newer Petersen et al mechanism was selected and modified to include the GRI-Mech 3.0 NO_x mechanism. The overall mechanism is somewhat large at 135 species and 771 reactions, but is expected to have excellent high pressure prediction of methane-hydrogen mixture combustion along with good NO_x prediction.

4.3 Experimental Setup

The experimental data used for this validation was conducted by [6] and entailed combusting a simulated biomass derived producer gas in a 3-cylinder Kubota D905 engine. The original 3-cylinder CI Kubota engine was modified to run in single cylinder (central cylinder) HCCI mode. The Kubota engine uses an indirect injection system where fuel is injected into a pre-chamber volume above the cylinder. Engine speed was maintained using an AC motor connected to a variable speed drive along with a resistive brake. Air intake heaters were used to maintain initial mixture temperature and thermocouples were placed along intake and exhaust streams to obtain temperature measurements. A piezoelectric pressure transducer was mounted in the original glowplug hole and used in conjunction with a 0.1 CAD resolution optical encoder to measure pressure-CAD data which was acquired with a Combustion Analysis System. Finally, emissions were measured using a MicroGasTM 5-gas analyzer. The experimental pressure traces are averaged over 125 consecutive cycles [6].

Two simulated biomass derived gas mixtures were run with this apparatus at varying equivalence ratios. Both mixtures vary in only their CO and H_2 concentrations. The fuel

mixture compositions (gravimetric) are shown in Table 4 and the engine running conditions are shown in Table 5.

Table 4: Mixture compositions

	CO	H_2	CH_4	CO_2	N_2
Mixture 1	25%	10%	2%	5%	58%
Mixture 2	20%	15%	2%	5%	58%

Table 5: Engine running parameters

Parameter	Mixture	Value
Compression Ratio (-)	1 & 2	22:1
Bore (mm)	1 & 2	72.o
Stroke (mm)	1 & 2	73.6
Connecting Rod to Crank Arm Ratio (-)	1 & 2	3.152
Displacement Volume (L)	1 & 2	0.3
IVC (aBDC)	1 & 2	30˚
EVO (aBDC)	1 & 2	55˚
Engine Speed (RPM)	1 & 2	1500
EGR (%)	1 & 2	0
Coolant Temperature (˚C)	1 & 2	80.4 ± 2
Intake Temperature (˚C)	1	159.9
	2	139.2
Equivalence Ratio (-)	1	0.398, 0.434, 0.500
	2	0.389, 0.431, 0.491

4.4 Results

4.4.1 Calibration

The calibration process followed for this fuel was based on mixture 1 with T_{in}=159.9˚C and φ=0.434. Running the multizone model with the original unmodified initial conditions of the experimental engine (for T_{in}=159.9°C and φ=0.434 case) produced the pressure trace shown in

Figure 13. In this first run, residual gas, blow-by losses, and temperature stratification were not considered as these parameters are introduced and modeled during the model calibration process. It can be seen that the unmodified initial conditions over predict pressure rise rate and peak pressure. Additionally, ignition is significantly advanced and there is deviation in the expansion stroke due to too much energy remaining in the charge in comparison to the experimental results.

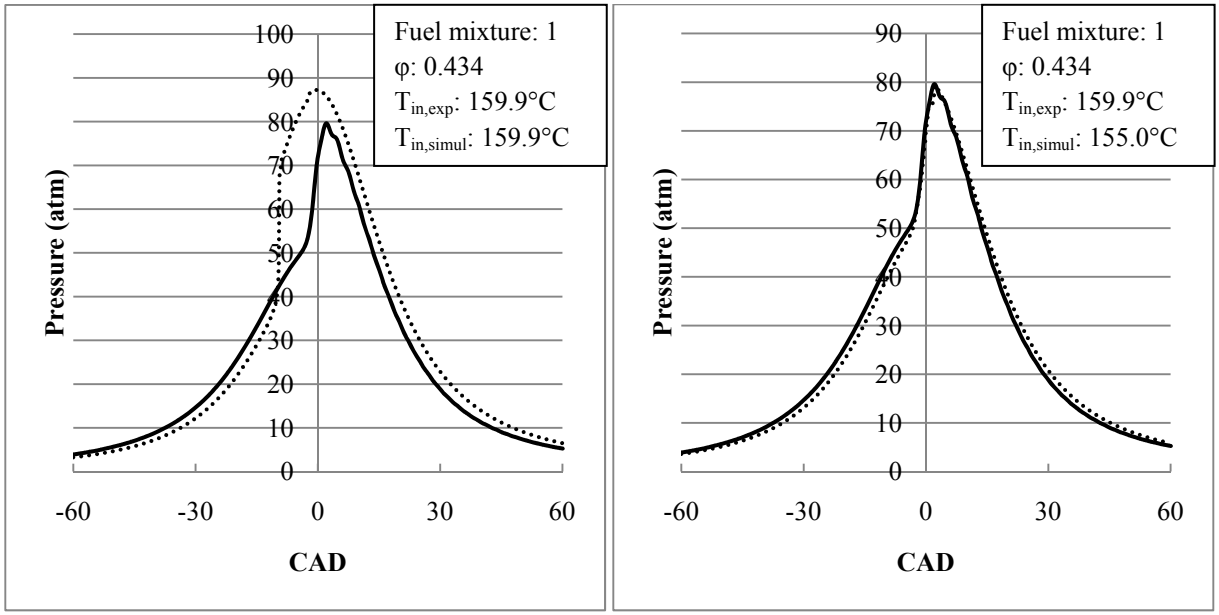

Figure 13: Simulation results using unadjusted model parameters (left). Calibrated results are on the right. Solid lines are experimental, dashed lines are numerical.

To calibrate the model for this operating point, initial changes involved matching the pressure traces during the compression stroke by adjusting blow-by losses. Ignition timing was then matched by adjusting the intake temperature of the mixture. Following this, other parameters such as geometric ratio, temperature stratification, and residual gas fraction were modified to achieve good pressure trace matching. Cylinder wall temperature was not directly measured, but was estimated to be 20 degrees above the coolant temperature to allow for heat transfer to occur. The calibrated pressure trace is shown in Figure 13. The final calibrated intake

temperature was 155°C which is very close to the experimental value of 159.9°C. The cooler calibrated intake temperature can be attributed to charge cooling as it enters the cylinder. Calibrated model parameters are shown in Table 6. It should be noted that both the experimental and numerical pressure traces do not exhibit two stage ignition which is characteristic of heavier hydrocarbon fuels commonly used in engines. This is because the heaviest hydrocarbon in the experimental fuel is CH_4 whereas the lightest hydrocarbon which displays two stage ignition is n-butane [3] [4].

Table 6: Calibrated multizone model parameters

Parameter	Mixture	Value
Intake Temperature (˚C)	1	155.0
	2	140.0
Wall Temperature (˚C)	1 & 2	100.0
Blow-by Constant (s^{-1})	1 & 2	6.0
Core zone Volume (%)	1 & 2	5
Residual gas Fraction (%)	1 & 2	12.5
Geometric Ratio (-)	1 & 2	1.0
Thermal Width (˚C)	1 & 2	30.0

4.4.2 Model Prediction

The calibrated model parameters were then applied to the other operating points for mixtures 1 and 2. This resulted in the pressure traces shown in Figure 14. When applying the model to mixture 2, the only parameters that were changed were mixture composition and intake temperature for the second set of simulation results. Both sets of results showed adequate matching between numerical and experimental pressure traces. However, for mixture 1, the case where φ=0.398 was over predicted by the simulation. This would tend to indicate that there was too much energy in the system in comparison with the experimental case. This may

be attributed to the fact that the experimental case is close to the misfire limit of the engine [6] and therefore has relatively more unburned or partially burned gas. Additionally, since the engine is close to the misfire limit, there will be an increase in cyclic variability [27]. One of the causes of cyclic variability is variation in the amount and composition of diluents [27]. In the case of operating near the misfire limit, or at very lean low load conditions, partially burned reactants can influence the composition of residual gases [79] which in turn can affect the composition of the subsequent engine cycle. This effect is shown in [27] where considerable cyclic variability is observed when the engine is operated near the misfire limit. Here, misfired cycles are followed by high energy release cycles due to large amounts of unburned reactants being carried forward by residual gases [27]. As mentioned earlier, the experimental pressure data used in this study are averaged over 125 cycles. The averaged dataset that results from this will mask the cyclic variability present and any significantly high or low pressure traces. Furthermore, the multizone model does not have the ability to predict cyclic variability. Thus, it would be difficult to predict the 125 cycle averaged experimental pressure trace for operating points very close to the misfire limit of the engine.

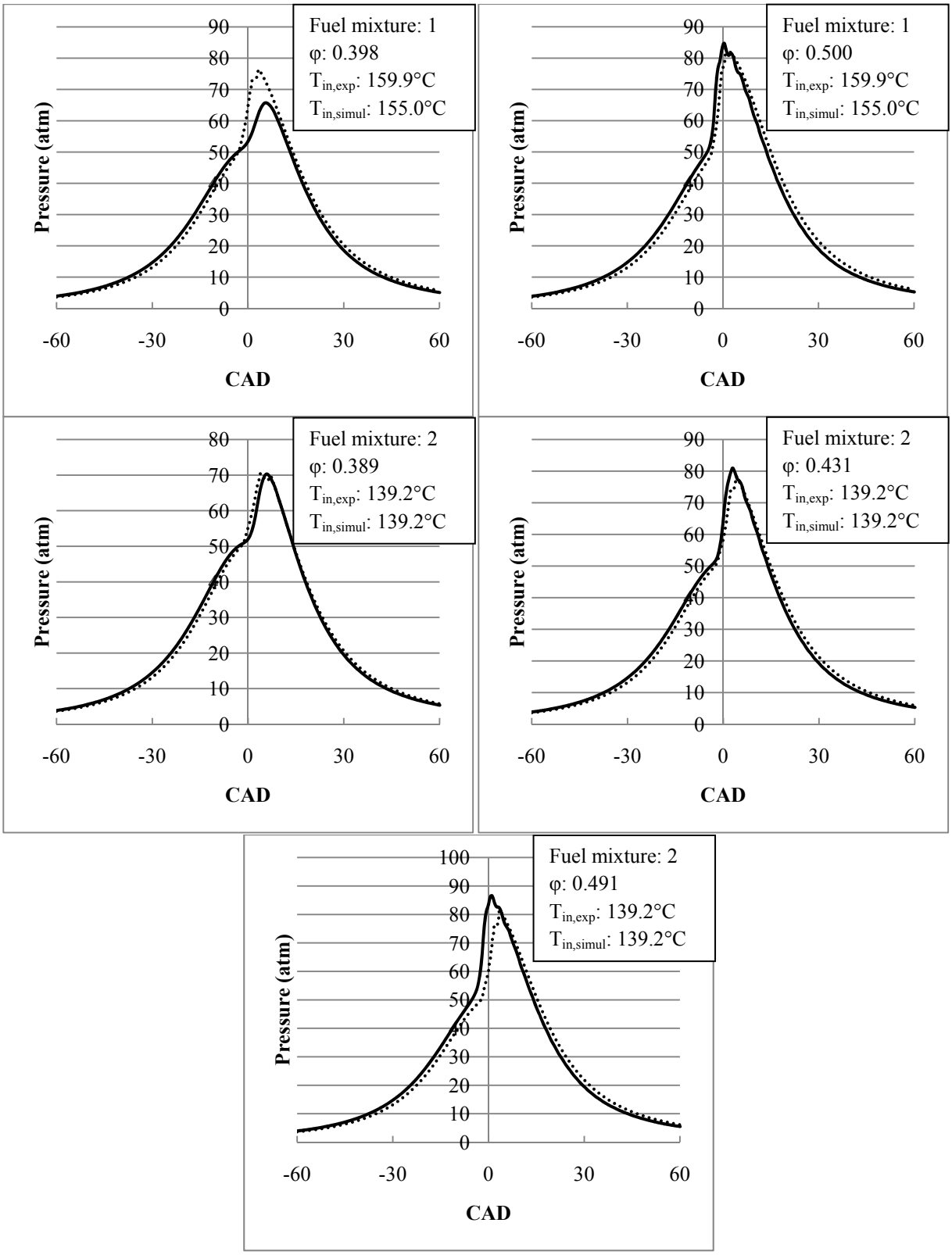

Figure 14: Simulated (dashed line) and experimental (solid line) pressure traces for various equivalence ratios, intake temperatures, and mixture compositions

Using these pressure versus CAD curves, heat release rate (HRR) were plotted. The heat release analysis method outlined in [36] was used. This method calculates the net HRR which accounts for any heat transfer through the walls of the cylinder. The HRR curve for the calibrated mixture 1 case (φ=0.434, Tin=159.9°C) is shown in Figure 15. The experimental and simulation HRRs match very well. Additionally, both curves captured a secondary peak after the bulk of the charge ignites. This secondary peak is somewhat difficult to observe in the pressure traces, but it is much more prominent in the HRR curves. In the simulation, this secondary peak is caused by the zone adjacent to the outermost near-wall zone experiencing slightly delayed ignition due to its cool temperature. It is not cool enough to not undergo combustion, but it is significantly cooler than the bulk charge by TDC of the piston. This can be seen in the cylinder temperature profile presented later in this paper (Figure 18). Once the bulk charge has ignited, the increased temperature and pressure incurred by this causes this cool zone to ignite, albeit after a short delay. However, the near-wall zone does not ignite. A similar situation likely occurred in the experimental engine where the bulk of the charge underwent ignition and burned in the pre-chamber, followed briefly by ignition and combustion of a slightly cooler charge that remained in the cylinder. This same trend can be seen in many of the other HRR curves and is well captured by the simulation which indicates that this multizone model is useful for capturing certain physical processes of HCCI combustion.

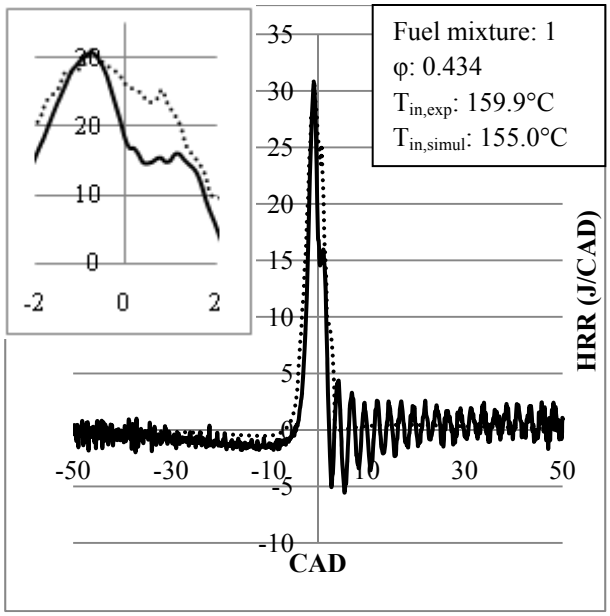

Figure 15: HRR curve for calibrated case – solid line is experimental, dashed line is simulation

The following plot (Figure 16) presents HRR curves for mixture 1 and 2 at the remaining equivalence ratios. As indicated above, for the case where φ=0.398, pressure was over predicted by the model and was likely due to too much energy being released and operating near the misfire limit of the engine where the model is unable to take cyclic variability into account. This is corroborated in Figure 16 where the simulated HRR is significantly higher than that of the experiment implying that there is simply too much energy being liberated via combustion in comparison to the experimental curve which is based on a 125 cycle pressure trace average.

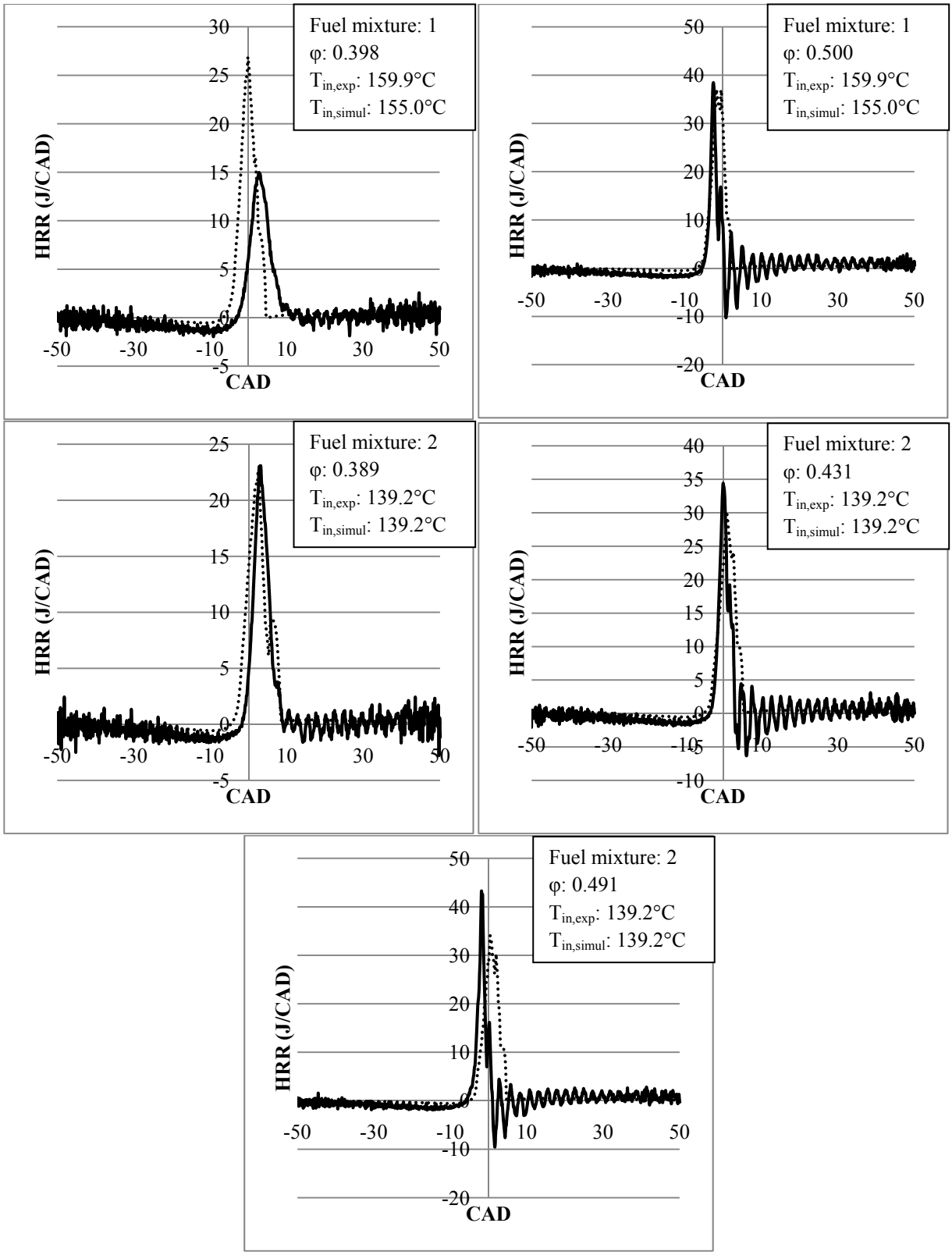

Figure 16: HRR curves for the remaining operating points. Dashed lines are simulation, solid lines are experimental.

4.4.3 Emissions

Analysis of the experimental data showed a maximum of approximately 11000ppm combined CO and UHCs and 15ppm NO_x present in the emissions [6]. Such low levels of NO_x are expected as HCCI combustion is a relatively low temperature process with no localized high temperature regions. Additionally, the simulated biomass gas used has no fuel bound nitrogen unlike liquid distillate fuels which can contain from 0.06% to 1.8% nitrogen depending on the grade [3]. This therefore limits NO_x production to mainly the prompt mechanism. However, the simulation results indicate NO_x levels ranging from 7 to 188ppm depending on the engine operating point as shown in Table 7. Such high NO_x levels may be due in part to the relatively high predicted peak in-cylinder combustion temperatures of approximately 2200K. There is no experimental in-cylinder temperature data available, but it is likely that the temperature has been somewhat over predicted by the model as peak HCCI combustion temperatures are around 1900K [80]. Furthermore, in indirect injection diesel engines such as the Kubota D905 used in the experimental work, squish area on the cylinder head increases local gas velocities and this can lead to higher thermal losses [36]. Such localized losses will not be captured by the Woschni correlation used to predict heat transfer in this numerical model so in-cylinder temperatures are likely over predicted.

Table 7: Emissions comparison for simulation and experimental cases

			NO_x		UHC + CO	
Mixture	**T_{intake}(°C)**	**φ**	**Simulation (ppm)**	**Experimental (ppm)**	**Simulation (ppm)**	**Experimental (ppm)**
1	159.9	0.398	24	4	7864	11024
1	159.9	0.434	54	7	8272	8470
1	159.9	0.500	188	0	8961	9823
2	139.2	0.389	7	5	6333	7874
2	139.2	0.431	22	6	6711	7373
2	139.2	0.491	66	14.5	7252	7226

NO_x production via the thermal route becomes dominant once temperatures exceed 1850K [3] so any over prediction of in-cylinder temperatures can have a significant impact on predicted NO_x levels – moreso if experimental temperatures are very close to or below the 1850K threshold. As shown below in this report, an increase in predicted peak in-cylinder temperature can result in a large increase in NO_x levels. Another reason why NO_x levels are over predicted may be due to the use of GRI-Mech 3.0 as a source for the NO_x mechanism. Studies [81] [82] [83] have shown that the GRI-Mech 3.0 mechanism can over predict NO_x levels by as much as two-fold over GRI-2.11 and measurement data.

Further analysis was done to determine the NO_x trends predicted by the numerical model. For mixture 1, at an intake temperature of 155.0°C, the upper limit of the engine operating range was found to be approximately at φ=0.500 and the lower limit was at φ=0.398 [6]. Selecting additional operating points between the three experimental cases (0.398, 0.434, and 0.500) and using the multizone model can give an idea of the NO_x trends that occur throughout the operating range for a fixed intake temperature. Additional equivalence ratios of φ=0.425, 0.450, and 0.475 were chosen and the predicted NO_x levels are shown below in Figure 17.

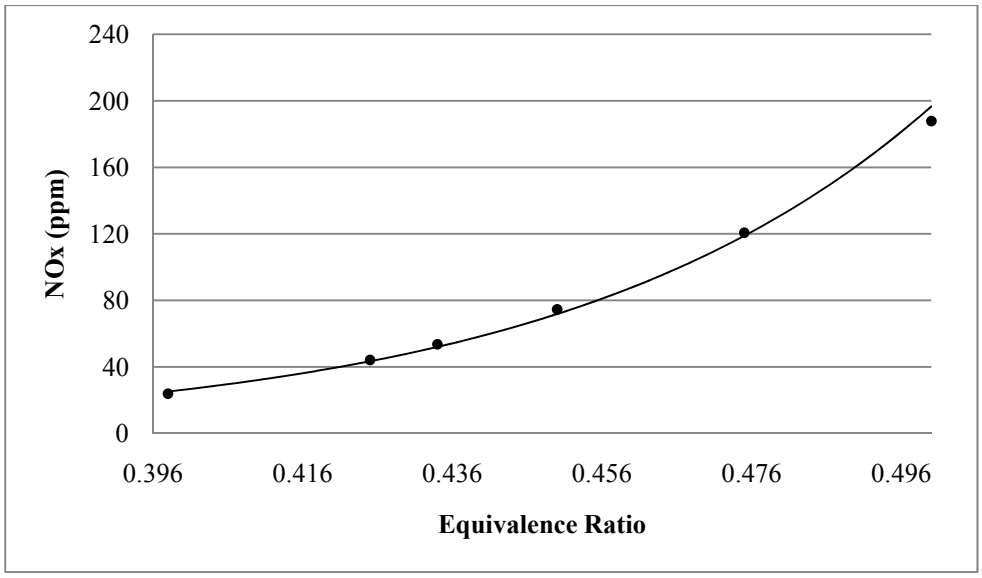

Figure 17: Simulated NO_x levels as equivalence ratio is increased for mixture 1 - T_{in}=155.0°C

The upward trend in NO_x levels can clearly be seen as the equivalence ratio is increased. This is expected since higher equivalence ratios indicate richer mixtures which means higher in-cylinder temperatures. The primary methods of NO_x formation in this situation are likely thermal and prompt as there is no fuel bound nitrogen, though the thermal mechanism will be dominant since the model is over predicting temperature. Depending on the equivalence ratio, predicted peak in-cylinder temperatures range from approximately 2100K to 2300K as shown in Table 8 which is approaching SI engine flame temperatures [36]. The thermal NO_x mechanism becomes active at around 1850K [3] so it is likely that much of the generated NO_x is via the thermal route as there is a very strong correlation with temperature. Additionally, the correlation is exponential which further corroborates the idea that the majority of NO_x production is via the thermal mechanism [3].

Table 8: Predicted NO_x levels compared to predicted peak in-cylinder temperatures

Predicted NO_x (ppm)	Predicted Peak Temperature (K)
24	2097
44	2144
54	2159
75	2184
121	2221
188	2256

This NO_x profile indicates that as in-cylinder temperatures rise, NO_x levels increase very rapidly. Therefore, when comparing simulation to experimental results, any over prediction in in-cylinder temperatures will have a significant impact on the predicted NO_x levels. For example, for the case of φ=0.398, the maximum predicted temperature is almost 2100K and NO_x levels are under 25ppm. However, at φ=0.500 peak predicted temperatures are almost at 2300K whereas NO_x levels reach 188ppm. So a relatively small increase of 200K gives rise to a large increase in NO_x emissions due to the exponential nature of the thermal mechanism once it reaches its activation temperature. Thus even a small over prediction in temperature can lead to very skewed NO_x predictions. Nevertheless, this model does correctly predict the NO_x trends that are expected to occur for increases in temperature.

As mentioned above, combined CO and UHC emissions peak on the order of 11000ppm in the exhaust gases of the experimental work. These gases are indicative of incomplete combustion. In HCCI engines, the bulk of incomplete combustion products are generated in the boundary layer that develops along in-cylinder surfaces and the crevice regions of the engine. These areas are cooler than the bulk charge due to their close proximity to cylinder walls and thus do not completely burn. The results from the numerical simulation results indicate a maximum of approximately 9000ppm combined CO and UHC emissions as shown in Table 7. Looking at

the temperature profile predicted by the simulation across the cylinder at TDC (Figure 18) and the temperature histories of the zones (Figure 19) it is clear that this same cool boundary layer occurs. Comparing combined CO and UHC emissions for each zone confirms that the vast majority of these emissions are produced in the outermost zone which represents crevice volume and the thermal boundary layer; which agrees with several other experimental and numerical HCCI studies [4] [17] [25] [43] [46]. In fact, zones 1 to 9 were found to contribute less than 0.01% of the combined incomplete combustion products.

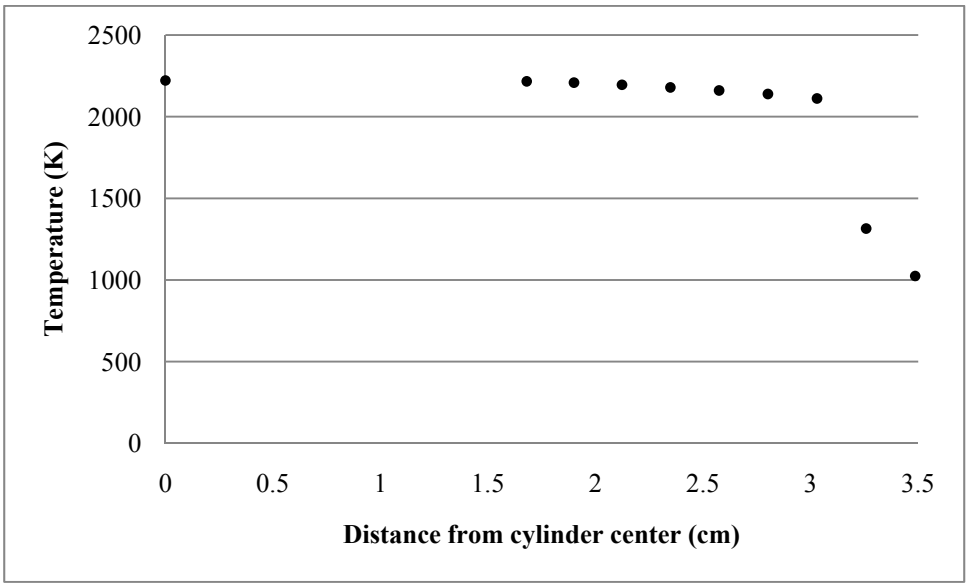

Figure 18: Temperature across a cross-section of the cylinder – 0 denotes the cylinder axis

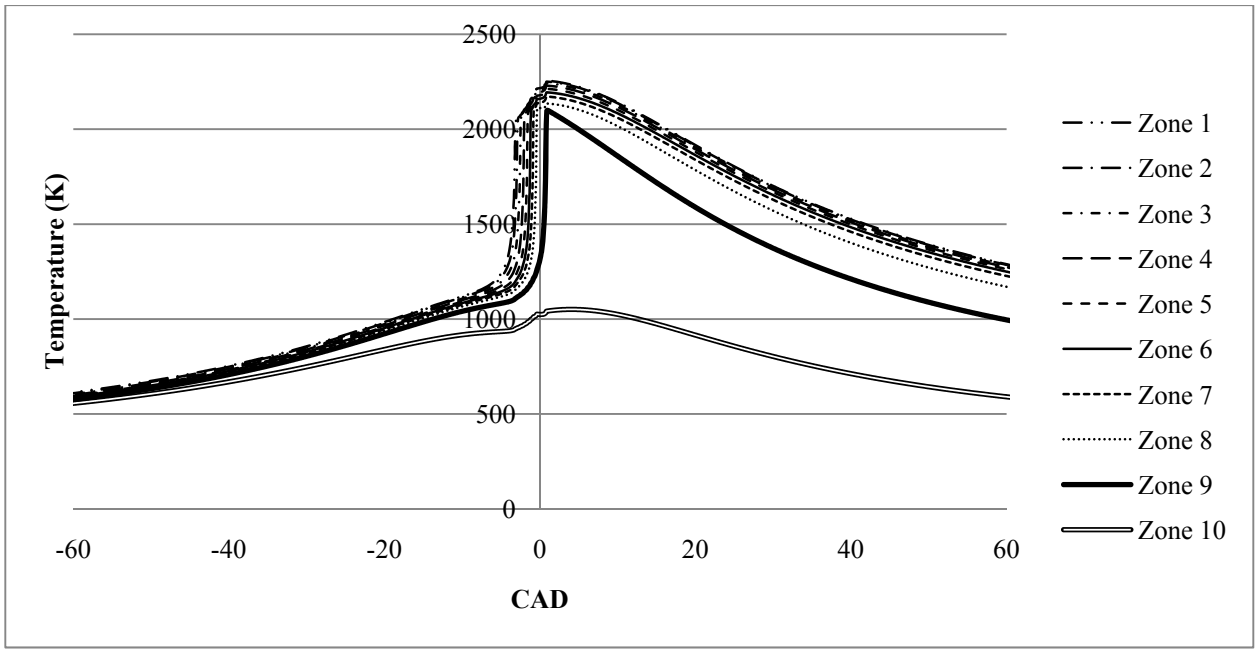

Figure 19: Zone temperature histories

Chapter 5: Biobutanol/n-heptane Validation

5.1 Biobutanol

Another renewable fuel that has seen limited use in HCCI engine work is biobutanol. Biobutanol is a biomass derived alcohol that is chemically identical to n-butanol derived from petrochemical sources [84]. It has an energy content of approximately27MJ/L [85] [86] which is higher than that of ethanol and closer to that of gasoline [84]. Biobutanol is primarily produced through ABE fermentation of biomass feedstocks using certain organisms of the genus Clostridium, notably *Clostridium acetobutylicum* [87]. To reduce cost and potential price increases of food crops, primary sources of biomass are second generation feedstocks which include agricultural wastes and wood residues [85] [87].

Biobutanol can readily be blended with gasoline and used in SI engines [84] [88]. As of this report, there has been limited work with regards to HCCI engines fuelled with biobutanol blends, but the work that has been done shows that it is a viable fuel option [26] [31]. Furthermore, simulation work of HCCI engines fuelled with biobutanol is lacking and there is very little work, if any, that has been conducted in this area.

5.2 Reaction Kinetics

The chemical mechanism chosen for this fuel was the semi-detailed model created by Dagaut and Togbe [86] as they were the only authors who had published a combined butanol/n-heptane mechanism. It is based on the amalgamation and reduction of two discrete models: an n-butanol model [20] and two n-heptane models [89] [90] [91]. The semi-detailed n-butanol/n-heptane mechanism was 181 species and 1703 reactions while the detailed scheme they

generated was 573 species and 2701 reactions. Both schemes were validated with two different molar fuel ratios, 20:80 and 50:50 (n-butanol:n-heptane). Experimental validation work was conducted over a range of temperatures from 530-1070K, at a pressure of 10 atmospheres, and equivalence ratios of 0.5 and 1.0 in a JSR. Good agreement was found between experimental results and the detailed mechanism but less accurate agreement was found when using the semi-detailed scheme. Nevertheless, it was recommended that the semi-detailed scheme be used for engine modeling due to its reduced complexity [86]. However, it should be noted that these validation test conditions are quite different from typical HCCI engine operating conditions, especially in terms of pressure and equivalence ratio.

Neither of the two proposed mechanisms contained a NO_x mechanism, thus the NO_x mechanism from GRI-Mech 2.11 [92] was combined with Dagaut and Togbe's mechanism to create a semi-detailed n-butanol/n-heptane with NO_x mechanism consisting of 200 species and 1805 reactions. The GRI-Mech 2.11 NO_x mechanism was selected as opposed to that from GRI-Mech 3.0 since previous work [81] [82] [83] [93] have indicated that GRI-Mech 3.0 may over predict NO_x levels.

5.3 Experimental Data Set

The experimental data for this validation set was conducted by [26] and involved combusting an n-butanol and n-heptane blend in a single cylinder HCCI engine. The engine test bed was a single cylinder Ricardo Hydra Mark III using a Mercedes E550 cylinder head with variable valve timing. Fuel was injected onto the backs of the intake valves using two separate systems, one for each fuel. Intake air was pressurized using an electric motor driven supercharger and intake temperature was set using a 600W electrical band-type heater. In-cylinder pressure measurements were taken using a Kistler water cooled piezoelectric sensor mounted flush

within the cylinder head. Intake temperature was monitored using a K-type thermocouple in the intake manifold with an accuracy of 2˚C. Exhaust emissions were measured using a 5-gas emissions test bench. NO_x emissions were measured with 1ppm resolution, UHCs with 10ppm resolution, and CO with 0.01% resolution. Crank angle position was recorded at 0.1˚ resolution using a BEI optical encoder.

Using this setup, varying butanol volume percentages (BVP) of fuel were tested at various equivalence ratios. Intake temperature and engine speed were held nearly constant at 80˚C and 1021RPM respectively. For this report, 5 operating points were selected - BVP12 (φ=0.332, 0.346), BVP17 (φ=0.345, 0.357) and BVP22 (φ=0.366). The operating conditions of the engine are presented in Table 9.

Table 9: Engine operating parameters

Parameter	Value
Compression Ratio (-)	12:1
Bore (mm)	97
Stroke (mm)	88.9
Connecting Rod to Crank Arm ratio (-)	3.5996
Displacement Volume (l)	0.653
IVO, IVC (aBDC)	151˚, 21˚
EVO, EVC (aBDC)	-100˚, 130˚
Engine Speed (RPM)	1021
EGR (%)	0
Coolant Temperature (°C)	69-70
Intake Temperature (°C)	80
Equivalence ratio (-)	0.332, 0.345, 0.346, 0.357, 0.366
BVP (%)	12, 17, 22

5.4 Results

5.4.1 Calibration

BVP 17, φ=0.357 was selected as the calibration case. Once again, the calibration process involved matching pressure traces during the compression stroke by adjusting blow-by and matching ignition timing through intake temperature. Following this, other parameters such as geometric ratio, temperature stratification, and intake temperature were further modified to achieve good pressure trace prediction. However, during the calibration process, intake charge temperature specification was not limited to being close to the measured intake manifold temperature due to the significant amount of trapped gas present in this engine which causes charge preheating. Additionally, it was found that blow-by was negligible during modeling and this is confirmed by [32]. The uncalibrated and calibrated pressure traces are shown in Figure 20. The uncalibrated pressure trace does not model residual gases, blow-by losses, and temperature stratification. Calibrated parameter inputs for the model are specified in Table 10. It should be noted that the high residual gas fraction of 29% is due to the early closing of the exhaust valve to trap hot residuals through NVO. Once again, cylinder wall temperature was not directly measured, but was estimated to be 20 degrees above the coolant temperature to allow for heat transfer to occur.

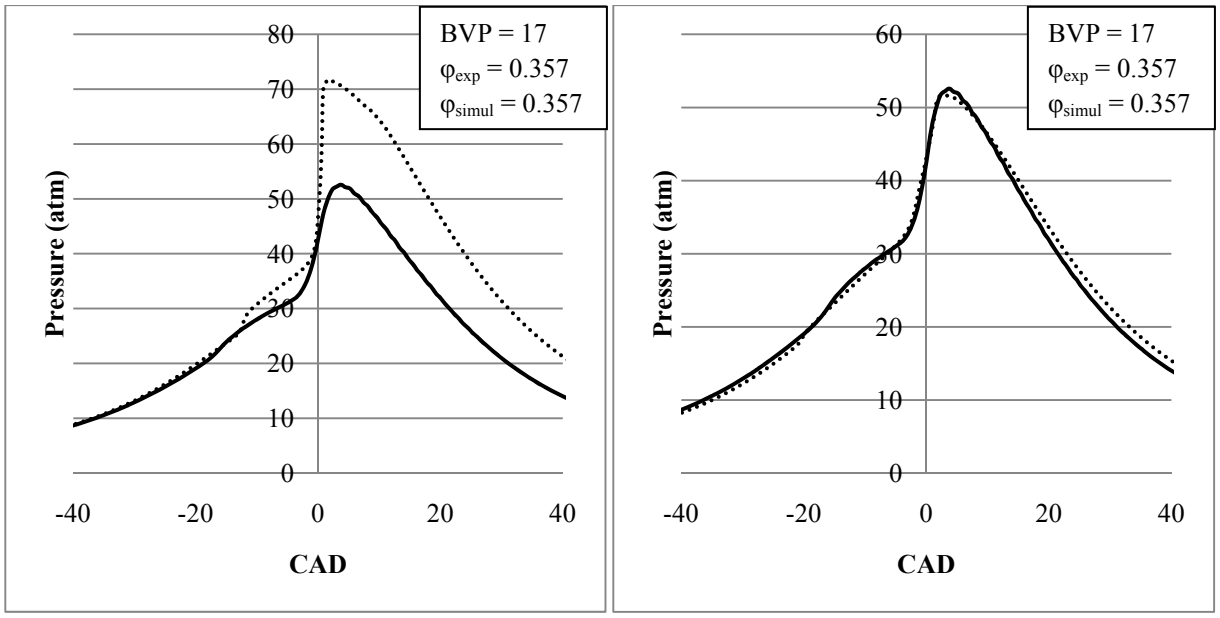

Figure 20: Uncalibrated (left) and calibrated (right) results. Dashed lines are simulation, solid are experimental.

Table 10: Calibrated model parameters

Parameter	Value
Intake Temperature (°C)	122
Wall Temperature (°C)	90.0
Core zone Volume (%)	30
Residual gas Fraction (%)	29
Geometric Ratio (-)	1.0
Thermal Width (°C)	0.0

Using this pressure curve, a heat release rate (HRR) curve was plotted as shown in Figure 21 using Heywood's method [36]. The HRR curve generally shows adequate matching though first stage ignition was somewhat early and larger than in the experimental data. Experimentally, first stage ignition peaks at around 15CAD bTDC whereas the simulation data indicates a peak at 20CAD bTDC. This difference may be attributed to the fact that the

calibrated input parameters are not measured values and thus any deviation from the actual values may be a cause for this error.

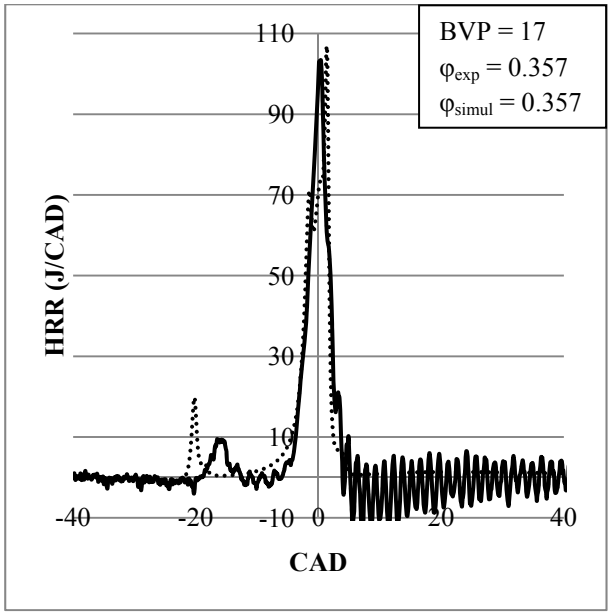

Figure 21: HRR curve for calibration case. Solid line is experimental, dashed is simulation

Experimental NO_x levels for the calibration case were 5.4ppm [26] while simulation results were 0.7ppm. The differences are likely due to the use of NVO in the experimental engine. As will be discussed later in this study, NVO can introduce significant amounts of inhomogeneities into the charge prior to ignition [11]. These inhomogeneities are due to stratification of both temperature and species concentrations. Any fuel rich regions caused by this could cause localized production of NO_x which would not be captured by the simulation due to its inherent assumption of complete mixing between trapped gasses and the inducted charge and the assumption that trapped residuals are at the same temperature of the intake charge.

Combined UHC and CO prediction for the calibration case was approximately 226ppm while the experimental UHC and CO levels were 3513ppm. The difference in levels is likely due to

the thermal boundary layer in the numerical model being too thin. This was observed during the calibration process of the model when the expansion stroke of the simulation showed some deviation from that of the experimental case. The deviation was caused by excess energy remaining in the charge and can be reduced by increasing the size of the quenched thermal boundary layer. However, increasing the size of this layer reduced the mass available for combustion and interfered with proper combustion. In the experimental case, the implementation of NVO facilitates combustion with fuel injection occurring during the NVO period [34] [56]. With NVO, trapped residuals can oxidize during the NVO period and fuel injected during this time facilitates combustion [34]. However, the simulation model only operates between IVC and EVO and will not capture the NVO period and its associated phenomena. Due to this, the combustion facilitation effect of NVO will not be captured and this did not permit an increase in the size of the thermal boundary layer.

5.4.2 Effect of NVO

Previous work [8] [93] involving this model did not use experimental data that implemented NVO, thus this is the first calibration attempt of this model using an engine with NVO. Due to the implementation of NVO, there can be variable amounts of trapped residual gases inside the cylinder depending on the valve timing. Using the experimental valve timing and engine specifications, the trapped gas percentage was determined using the ratio of volume at EVC to volume at IVC and was found to be 29%. This level of trapped gas is quite high but it is confirmed by other work using this same engine [32]. Such high levels of trapped gas occur because the exhaust valve is closed before the piston is near TDC thus preventing all the exhaust gas from being evacuated. These trapped gases can be at a fairly high temperature [11] and this can result in significant charge preheating. The inclusion of such a large percentage of

exhaust gases in the subsequent intake charge has different effects with regards to the model used in this study. Firstly, since the multizone model does not account for the temperature of trapped residual gases (it assumes trapped gases are at the same temperature of the intake charge), the intake charge temperature specified as an input for the model must be increased. Secondly, for this study, the initial calibration did not require temperature stratification at IVC and assumed a homogeneous mixture throughout the cylinder. However, in practice, NVO results in significant inhomogeneity and stratification of the charge temperature and trapped residual gas [11]. This can lead to fuel rich regions which will ignite sooner than if the charge were completely homogeneous. Increasing the overall equivalence ratio of the model can account for the earlier ignition caused by fuel rich regions and applying temperature stratification can better mimic the experimental situation. Finally, this model assumes trapped gases to constitute only of completely burned products whereas in practice, trapped residuals will have some UHCs. These recycled UHCs may contribute to combustion by effectively creating a slightly richer mixture in the subsequent cycle. This effect may be minimal for most operating points, but for points near the misfire limit, the recycling of unburned and partially burned reactants can significantly influence subsequent cycles [27]. So due to NVO, the energy content of the intake charge can be increased via the heat energy of the trapped residuals, and any unburned or partially oxidized reactants.

To attempt to better address this increased energy content and improve pressure trace matching, the calibration case (BVP 17, φ=0.357) was re-calibrated using fewer constraints on the calibration parameters to obtain a better match. The main difference between the experimental and original simulation pressure curves was a some deviation during the

expansion stroke likely due to too much energy remaining in the charge during expansion. This can be improved by forcing more mass into the outer zone to reduce the amount of mass which reacts. Doing so has two effects: it increases total unburned reactant emissions and reduces the peak pressure since there is less mass available for combustion. This helps improve unburned reactant emission prediction, but causes poor pressure prediction as observed earlier. To address this, the equivalence ratio needed to be increased by 14.8%. Not only did this aid in combustion, but it also represented the increase in equivalence ratio caused by trapped UHCs and any fuel rich regions which may ignite early. Normally, for engines not implementing NVO, the equivalence ratio is not adjusted and is set to the experimental value [8] [93]. Admittedly, a 14.8% increase is fairly large. Nevertheless, this increase, along with increased mass in the outer zone, was the primary difference between the new calibration and the original calibrated results. Along with other minor changes, this calibration resulted in excellent pressure trace matching for the calibration case as shown in Figure 22. Calibrated model parameters are shown in Table 11. Expansion stroke pressure trace matching was also improved compared to the original calibration. Using the pressure data, the HRR curve was generated and this showed excellent matching compared to the experimental results. In addition to exhibiting good peak behavior, the HRR curve showed significantly improved first stage combustion timing and magnitude.

Table 11: Calibrated model parameters

Parameter	Value
Intake Temperature (°C)	132
Wall Temperature (°C)	90.0
Core zone Volume (%)	1
Residual gas Fraction (%)	29
Geometric Ratio (-)	1.0
Thermal Width (°C)	30.0

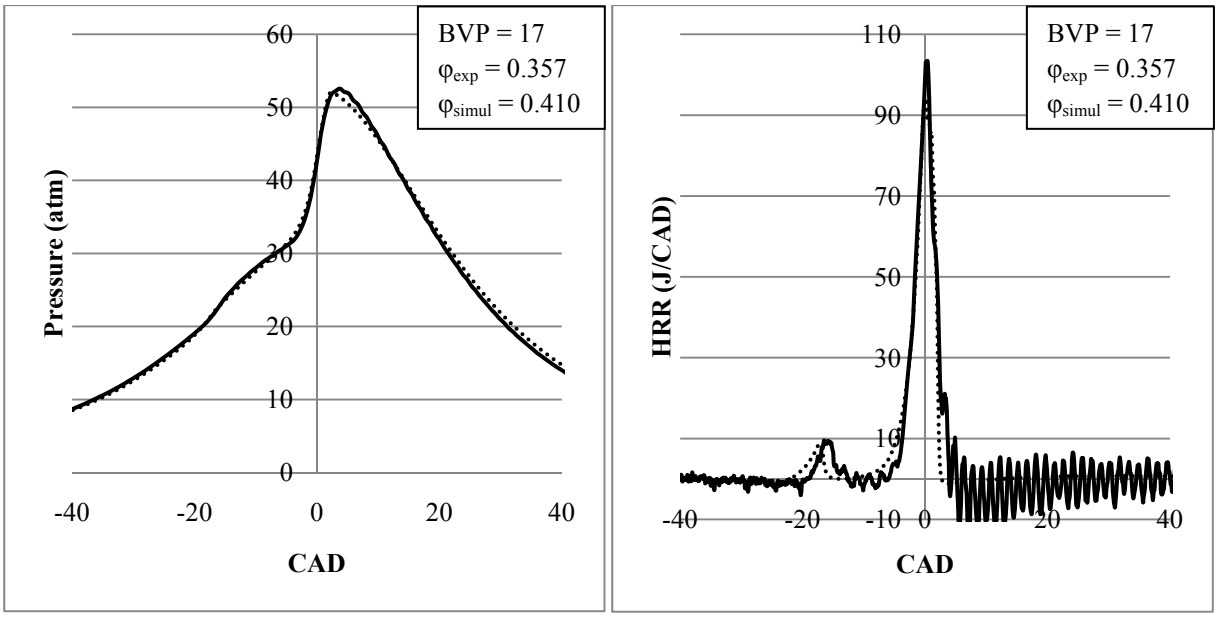

Figure 22: Pressure and HRR curves for improved calibration case. Solid lines are experimental, dashed are simulation.

5.4.3 Model Predictions

Using this new set of calibrated parameters, the other four operating points of interest were modeled. No parameters were changed during the modeling except for BVP and the equivalence ratio. However, all equivalence ratios maintained a 14.8% increase, similar to the calibration case. All predictive pressure traces for the 4 operating points showed good matching as shown in Figure 23. However, there is still a very small amount of deviation during the expansion strokes of the predicted pressure traces. Nevertheless, the simulation results capture the overall trends of the system with good prediction of cool flame activity. For example, moving from φ=0.332 to φ=0.346 with BVP12 shows an increase in peak pressure which is expected due to the richer mixture, though low temperature heat release seems to be very similar. Further analysis of the effect of increasing equivalence ratios on cool flame activity for a given BVP will be discussed later.

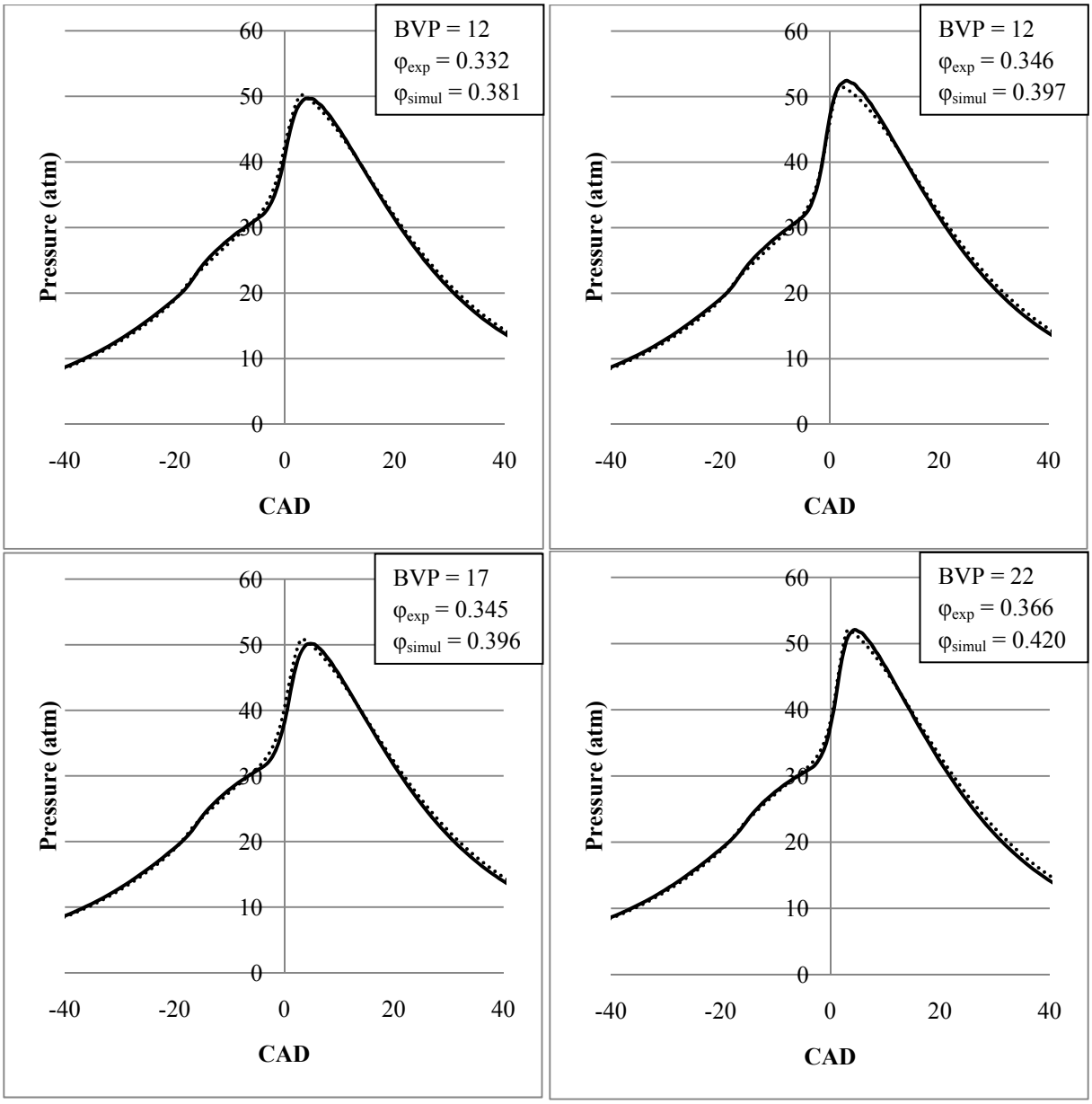

Figure 23: Predicted pressure traces for 4 operating points. Solid line is experimental, dashed is simulation.

Based on these pressure curves, the HRR curves shown in Figure 24 were plotted. All curves show excellent main ignition timing and magnitude and very good low temperature heat release timing and magnitude.

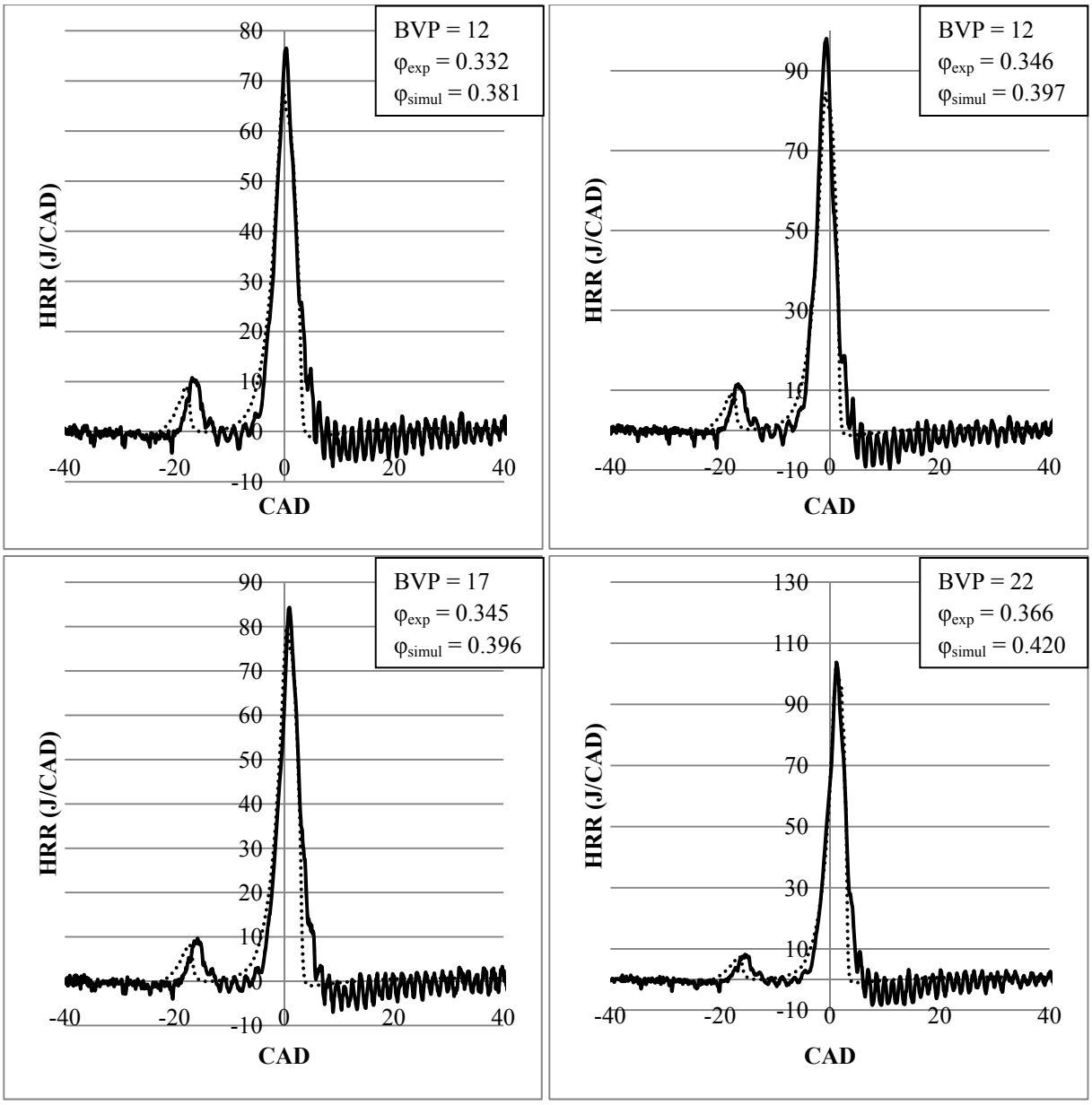

Figure 24: HRR curves for 4 operating points. Solid line is experimental, dashed is simulation.

The experimental work upon which this paper is based indicates that for a given BVP, HRR curves for various equivalence ratios showed nearly identical low temperature heat release, but varying high temperature heat release. In other words, equivalence ratio had little effect on cool flame activity for a given BVP. This same trend is observed in the simulation predictions. Along with running φ=0.332 and 0.346 for BVP12, three other simulation cases were run:

φ=0.320, 0.340, and 0.360. The HRR curves for these 5 cases are shown in Figure 25. From the data it is clear that varying the equivalence ratios for BVP12 showed very little change in the low temperature heat release.

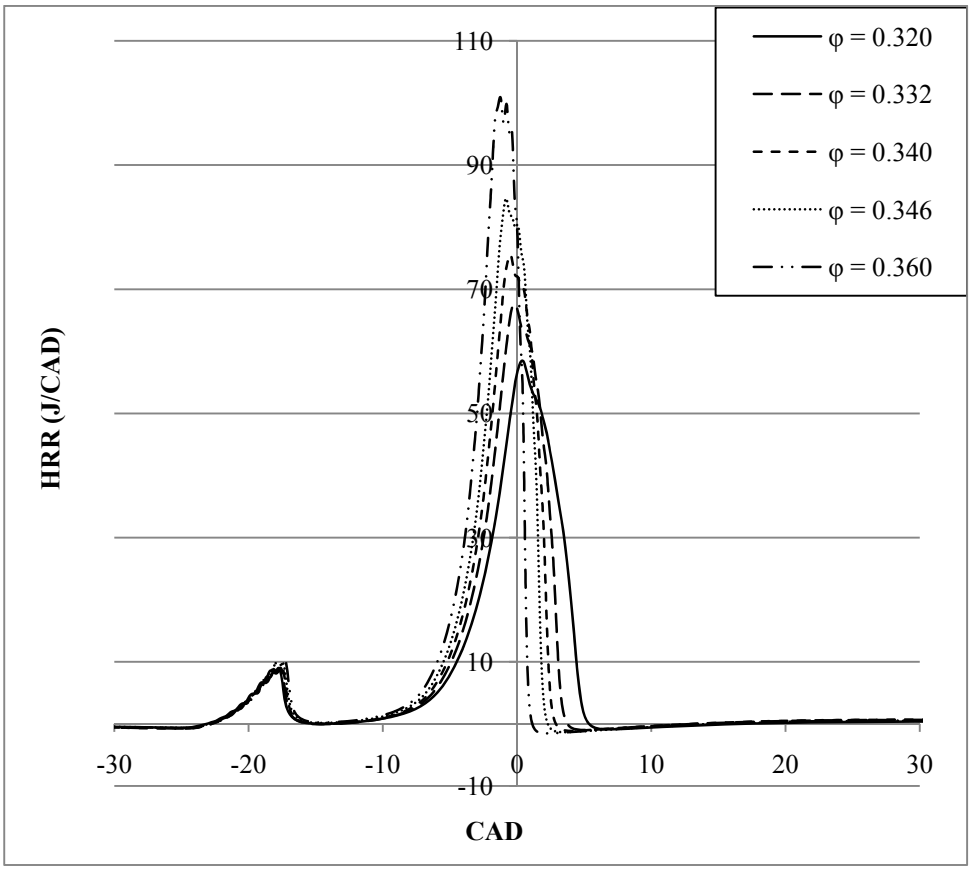

Figure 25: Varying equivalence ratios for BVP 12

5.4.4 Emissions

Combined UHC and CO prediction was improved and levels for the four predictive cases were on the order of 500ppm as shown in Table 12. These levels are better in comparison to the first set of calibration results due to increased mass in the outer zone, however, levels are still somewhat low as the experimental cases were around 3000 to 4000ppm. The main cause is once again lack of mass quenched in the thermal boundary layers. One possible method of addressing this is to incorporate mass transfer into the model as this would allow mass to move

into crevice and thermal boundary regions during the engine cycle and this would improve emissions predictions [45].

Table 12: Experimental and simulation emissions

		NO_x		UHC + CO	
BVP	**φ**	**Simulation ppm)**	**Experimental (ppm)**	**Simulation (ppm)**	**Experimental (ppm)**
12	0.3220	0.60	5.5	492	4347
12	0.3460	0.54	5.4	503	3678
17	0.3450	0.55	5.3	521	4036
17	0.3570	0.53	5.4	531	3513
22	0.3660	0.52	5.1	558	3588

NO_x emissions for all 4 predictive cases were approximately one order of magnitude below experimental values which were on the order of 5ppm. As previously mentioned the model cannot capture inhomogeneity in species concentrations, and this can lead to a certain degree of discrepancies in predicting chemical species and temperature in the engine. Considering the three mechanisms of NO_x formation, namely fuel, prompt, and thermal, NO_x formation from fuel sources is unlikely in this work as there is no fuel bound nitrogen. Prompt NO was not found in the simulation results as this mechanism has been primarily observed in fuel rich flames where hydrocarbon groups react with nitrogen to form HCN via $CH + N_2 \leftrightarrow HCN+N$ [94]. The only mechanism, therefore, is thermal NO_x. It is interesting to see that as BVP was increased, NO_x levels decreased (Figure 26) and [26] indicates that this is due to a reduction in peak in-cylinder temperatures though no temperature measurements were taken. This same trend is observed in the simulation results, however here the downward NO_x trend corresponded with a very slight increase in temperature for increasing BVPs – which is counter to the expected results from the thermal NO_x mechanism. This is caused by discrepancy in predicting certain chemical species such as N_2 and O_2 under engine conditions. It was found

that as BVP was increased, predicted N_2 and O_2 levels decreased. Since temperature only showed a very slight increase, reaction rate constants were fairly constant. Therefore, for decreasing concentrations of N_2 and O_2, overall NO production rates would decrease which would explain the downward trend. Again, the model has limitations in describing NVO equipped HCCI engines. Nevertheless, even though the simulation results under predict NO_x levels, the model is useful for capturing overall trends.

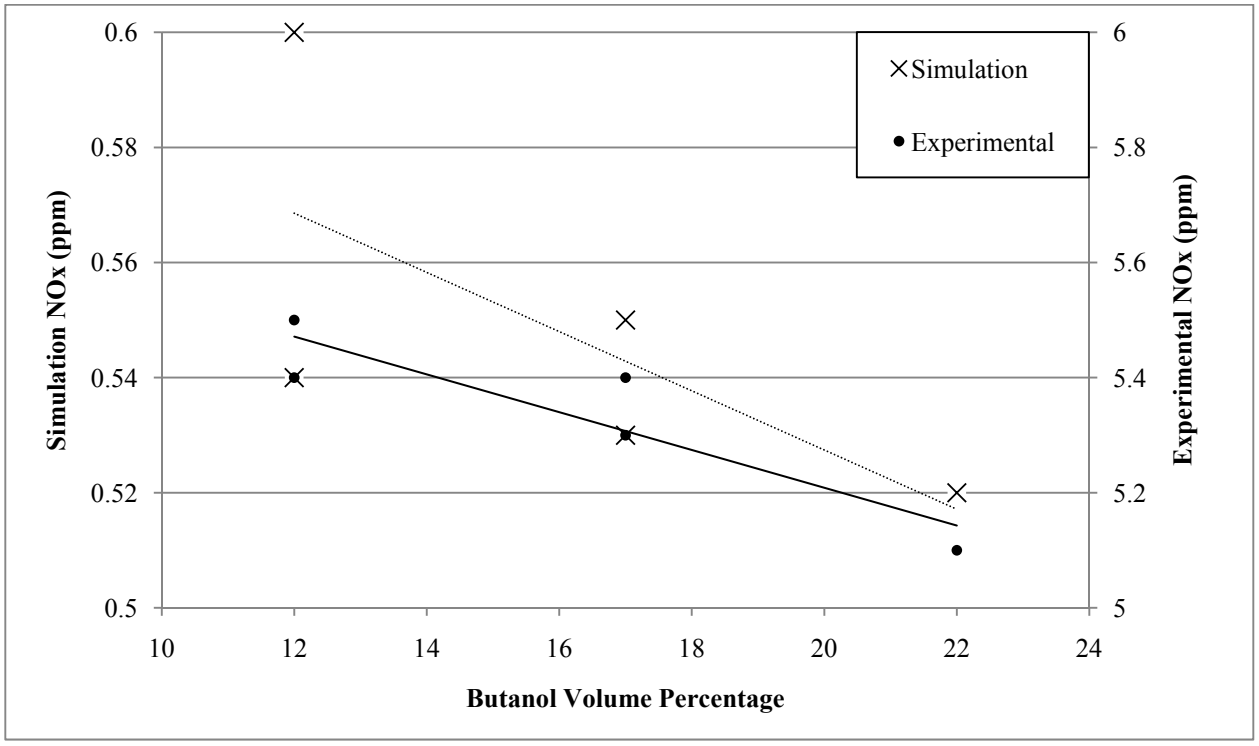

Figure 26: NO_x trends in experimental and simulation data for various butanol volume percentages

Chapter 6: Conclusions

For this thesis, a serial 10 zone numerical HCCI model was parallelized and validated using two sets of experimental data involving biofuels. Improvements to the original code included updating it to FORTRAN 90, compiling it as a 64bit application, and restructuring it to allow for ease of use. These changes allowed for a reduction in runtimes by approximately half for the various validation cases when running the model on a quadcore Intel i7 processor. It was also found that increasing the number of zones changed the overall system and would require recalibration of the model if one wanted to study the effect of increasing zones. Increasing the number of zones over 10 would not have presented significant gains in accuracy for the purpose of this study.

Two new sets of validation work were done using the improved numerical model. The first set involved a converted indirect injection diesel Kubota D905 engine fuelled with biomass derived gas. 6 engine operating points were chosen and upon calibration to one of them, the model generally showed good pressure prediction and HRR curves for the others. A secondary peak which was barely noticeable in the pressure data was well captured in many of the HRR curves of the simulation. This secondary peak is caused by cooler gases undergoing slightly delayed combustion and is likely caused by cooler gas that had ignited within the cylinder. However, the model had difficulty in predicting pressure traces when the operating point was near the misfire limit of the engine. The cause of this is that the model is unable to handle cyclic variability that occurs when the engine is operated near the misfire limit.

NO_x emissions were over predicted, however, the model did capture the trend of thermal NO_x. Additionally, relatively small increases in in-cylinder temperatures were found to bring about large increases in predicted NO_x levels which can be explained by the thermal NO_x mechanism. Thus, it is likely that the over prediction of NO_x is a result of over predicted in-cylinder temperatures. Products of incomplete combustion showed good matching. The vast majority of these products were generated by the outermost zone which is expected as UHC and CO production in HCCI combustion is due to crevice and thermal boundary zones. Overall, the model was shown to be fairly fast and robust in terms of predicting pressure, HRR, ignition timing, and emissions trends for a non-NVO equipped HCCI engine fuelled with biogas.

The second validation set for the improved model tested its limitations and involved calibrating it to a set of experimental data from a n-butanol/n-heptane fuelled HCCI engine utilizing NVO. 5 operating points were chosen for this and upon initial calibration the model showed weak prediction of the low temperature regime for hydrocarbon oxidation. However, once the model was recalibrated to account for some of the effects of NVO the simulated pressure traces were found to show good matching for all operating points tested. Similarly, subsequent HRR curves showed excellent matching as well, with notable improvements in the prediction of first stage ignition timing and magnitude.

Predicted NO_x emissions were found to be on the low side due to the lack of inhomogeneity in the model, though once again, overall NO_x trends were predicted. Similarly, UHC emissions

were low as well, however, they were improved after some of the effects of NVO were accounted for during calibration.

As expected, this model cannot completely capture the combustion benefits offered by the implementation of NVO due to the fact that it operates between the closed valve period following the intake stroke. However, calibration of the input parameters to account for some aspects of NVO did show better pressure trace and HRR prediction in the n-butanol/n-heptane validation. In conjunction with the biogas validation and previous work with the model, this would indicate that the model can be used as a predictive tool for in-cylinder pressure, heat release, and combustion phasing for HCCI engines fuelled with different biofuel blends.

Chapter 7: Recommendations

The major recommendations for improving the predictive capability of this model are listed below. Most of these are a significant deviation from the relatively simple approach taken in the current algorithm and would require the model to be completely redone.

Firstly, the model needs to incorporate mass transfer between zones along with a crevice region and thermal boundary layer to improve its predictive capabilities. The approach used here can be similar to the work done by [17] where conservation of mass equations were applied to boundary regions involved in mass transfer. This would allow for mass to be pushed into cooler regions and crevice volumes of the cylinder as is the case in experimental engines where over 35% of the charge mass can be pushed into cooler boundary regions [25]. Furthermore, mass transfer in multizone models can improve UHC and CO emissions prediction [12] along with the overall pressure behavior since heat release will be moderated. In the current model, a form of this can be done by controlling the size of the outermost zone and either assigning it a high heat transfer value (essentially keeping it non-reactive) or assigning sufficient temperature stratification that the outermost zone simply does not have enough initial energy to combust. However, this method can only work with a fixed amount of mass in this zone as there is no mass transfer implemented in the model and it is difficult to calibrate the size of this frozen volume.

A second area for improvement, which could be implemented with the current model, is to link a CFD solver that will run during the engine cycle up to IVC. Once the CFD solver generates a temperature and concentration field, these variables can be binned according to the zones in the multizone model and used as inputs. This would allow for improved initial conditions being

used for the model and would eliminate some of the calibration process. Currently, the calibration process is a lengthy task and eliminating part of it would add considerable value to the model. Additionally, since many experimental HCCI engines incorporate NVO, the CFD solver would be very beneficial in these situations in that it would be able to capture the significant charge and temperature inhomogeneities that arise. These inhomogeneities are difficult to capture through calibration. However, since the model uses a ring like zone distribution, some of the inhomogeneities will not be captured. Additionally, since fuel injection during the closed valve period is common in NVO, coupling the CFD solver with chemical kinetics is a further possibility to capture any low temperature chemical reactions that occur within the trapped gases at the end of the exhaust stroke once EVC has occurred. However, doing so would make the model more computationally intensive and at this point, one may simply implement chemical kinetics with CFD throughout the closed cycle period as well.

Finally, it is recommended that the model domain breakdown be altered from the current concentric ring approach to a lumped stirred reactor approach as shown in the figure below. For ideal HCCI engines where turbulence and mixing are assumed to be complete, a concentric ring division of the domain works well since there is a natural ring-like temperature stratification of the well mixed charge during compression [17]. However, with experimental engines, and most notably engines implementing NVO, stratification of the charge and temperature occurs in a non-symmetric fashion [9] [10] [11] and can be significant. Therefore, a more suitable way to model this would be using individually lumped stirred reactors as done by [35] [43].

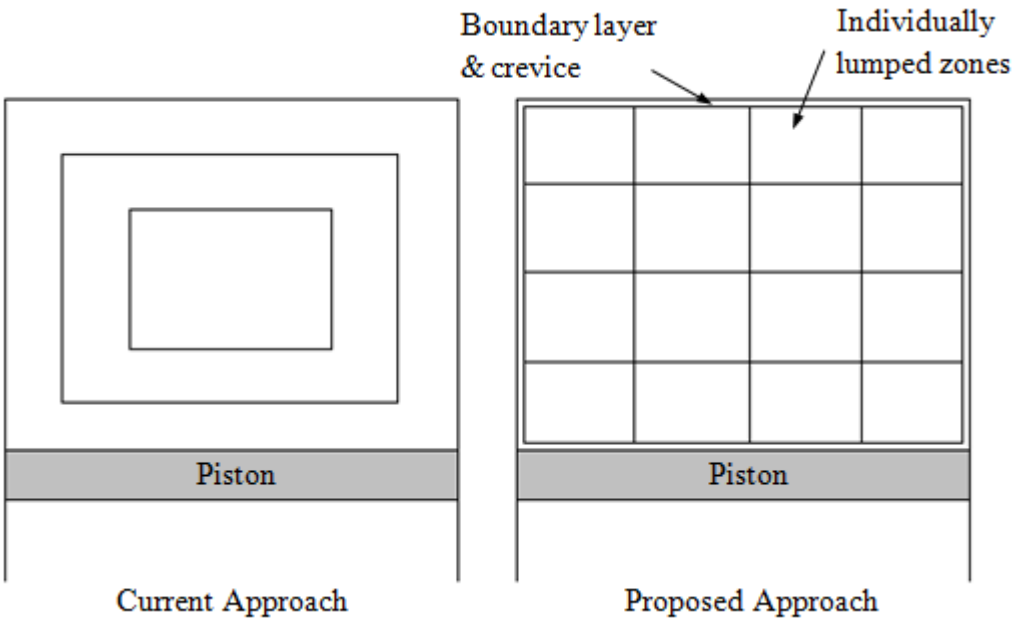

Figure 27: Zone distribution

This would offer a much more realistic simulation base for typical NVO equipped HCCI engines. An additional benefit of this method is that it would allow for multiple regions to ignite at once. Due to temperature stratification and colder cylinder walls, the current model generally initiates ignition at one zone (usually the core zone) and subsequent zones follow very closely. As indicated previously, this is an ideal case for a perfectly homogeneous situation. However, small inhomogeneities exist, and when NVO is implemented, these inhomogeneities become more widely distributed and more extreme. Not only will these cause ignition to occur at multiple points, but they can also be a source of NO_x emissions. Using a lumped stirred reactor approach would be of benefit in such a situation, and increasing the number of zones would allow for improved spatial resolution of the inhomogeneities thereby improving accuracy of the model. Spatial resolution could also only be increased in areas that have been proven to be sources of inhomogeneities such as near inlet and exhaust valves [11] to help reduce computational resources. Additionally, coupling this model with a CFD solver

would allow for proper binning of variables such as temperature and species into appropriate zones.

References

[1] **F. Vanek, L. Albright.** *Energy Systems Engineering: Evaluation & Implementation.* New York : McGraw Hill, 2008.

[2] *The feasibility and potential environmental benefits of alternative fuels for commercial aviation.* **J. Hileman, H. Wong, D. Oritz, N. Brown, L. Maurice, M. Rumizen.** Anchorage : 26th International Congress of the Aeronautical Sciences, 2008.

[3] **Lefebvre, A.** *Gas Turbine Combustion, 2nd Edition.* Ann Arbor, MI : Edwards Brothers, 1999.

[4] *Progress and recent trends in homogeneous charge compression ignition (HCCI) engines.* **M. Yao, Z. Zheng, H. Liu.** s.l. : Progress in Energy and Combustion Science, 2009, Vol. 35, pp. 398-437.

[5] *Study on Biomass Gas HCCI Engine.* **Y. Yamasaki, M. Kanno, Y. Taura, S. Kaneko.** 2009-32-0066, s.l. : SAE International, 2009.

[6] *Experimental indicated performance of a HCCI engine fuelled by simulated biomass gas.* **D. Haggith, A. Sobiesiak, L. Miller, G. Przybyla.** 2010-01-1081, s.l. : SAE International, 2010.

[7] *An experimental study of the biogas-diesel HCCI mode of engine operation.* **S. Swami Nathan, J. Mallikarjuna, A. Ramesh.** s.l. : Energy Conversion and Management, 2010, Vol. 51, pp. 1347-1353.

[8] *Knock limit prediction via multi-zone modelling of a primary reference fuel HCCI engine.* **T. Tzanetakis, P. Singh, J.-T. Chen, M. Thomson, C. Koch.** s.l. : International Journal of Vehicle Design, 2010, Vol. 54, pp. 47-72.

[9] *Characterizing the development of thermal stratification in an HCCI engine using planar-imgaing thermometry.* **J. Dec, W. Hwang.** 2009-01-0650, s.l. : SAE International, 2009.

[10] *An investigation of thermal stratification in HCCI engines using chemiluminescence imaging.* **J. Dec, W. Hwang, M. Sjoberg.** 2006-01-1518, s.l. : SAE International, 2006.

[11] *Simultaneous imaging of exhaust gas residuals and temperature during HCCI combustion.* **D. Rothamer, J. Snyder, R. Hanson, R. Steeper, R. Fitzgerald.** s.l. : Proceedings of the Combustion Institute, 2009, Vol. 32, pp. 2869-2876.

[12] *A comparative study of multi-zone combustion models for HCCI engines.* **M. Jia, M. Xie.** 2008-01-0064, s.l. : SAE International, 2008.

[13] *A study on gasoline engine combustion by observation of intermediate reactive products during combustion.* **M. Noguchi, T. Tanaka, Y. Takeuchi.** 790840, s.l. : SAE International, 1979.

[14] *Onset behavior of low-temperature flames caused by piston compression.* **M. Furutani, Y. Ohta, K. Komatsu.** s.l. : Japan Society for Automotive Engineers, 1993.

[15] *Combustion analysis of methanol-fueled active thermo-atmosphere combustion (ATAC) engine using a spectroscopic observation.* **Iida, N.** 940684, s.l. : SAE International, 1994.

[16] *An experimental study on premixed-charge compression ignition gasoline engine.* **T. Aoyama, Y. Hattori, J. Mizuta, Y. Sato.** 960081, s.l. : SAE International, 1996.

[17] *A multi-zone model for prediction of HCCI combustion and emissions.* **S. Aceves, D. Flowers, C. Westbrook, J. Smith, W. Pitz.** 2000-01-0327, s.l. : SAE International, 2000.

[18] *Spectroscopic measurements of low-temperature heat release for homogeneous combustion compression ingition (HCCI) n-heptane/alcohol mixture combustion.* **P. Saisirirat, F. Foucher, S. Chanchaona, C. Mounaim-Rousselle.** s.l. : Energy & Fuels, 2010, Vol. 24, pp. 5404-5409.

[19] *Auto-ignition and combustion characterisitics in HCCI and JSR using 1-butanol/n-heptane and ethanol/n-heptane blends.* **P. Saisirirat, C. Togbe, S. Chanchaona, F. Foucher, C. Mounaim-Rousselle, P. Dagaut.** s.l. : Proceedings of the Combustion Institute, 2011, Vol. 33, pp. 3007-3014.

[20] *Oxidation kinetics of butanol-gasoline surrogate mixtures in a jet-stirred reactor: Experimental and modeling study.* **P. Dagaut, C. Togbe.** s.l. : Fuel, 2008, Vol. 87, pp. 3313-3321.

[21] News Release. *GM Demonstrates Fuel-Saving Engine Technology Breakthrough with HCCI-Enabled Saturn Aura Concept.* [Online] GM, May 5, 2008. [Cited: October 12, 2010.] http://archives.media.gm.com/archive/documents/domain_39/docId_45489_pr.html.

[22] *Experimental studies on controlled auto-ignition (CAI) combustion of gasoline in a 4-stroke engine.* **A. Oakley, H. Zhao, N. Ladommatos, T. Ma.** 2001-01-1030, s.l. : SAE International, 2001.

[23] *Homogeneous charge compression ignition (HCCI) using isooctane, ehtanol and natural gas - a comparison with spark ignition operation.* **M. Christensen, B. Johansson, P. Einewall.** 972874, s.l. : SAE International, 1997.

[24] *HCCI operation of a dual-fuel natural gas engine for improved fuel efficiency and ultra-low NOx emissions at low to moderate engine loads.* **R. Stanglmaier, T. Ryan III, J. Souder.** 2001-01-1897, s.l. : SAE International, 2001.

[25] *Modeling of HCCI combustion and emissions using detailed chemistry.* **W. Easley, A. Agarwal, G. Lavoie.** 2001-01-1029, s.l. : SAE International, 2001.

[26] *Combustion characteristics of butanol/n-heptane blend fuels in an HCCI engine.* **M. Shahbakhti, A. Ghazimirsaied, A. Audet, C. Koch.** Ottawa : Proceedings of Combustion Institute - Canadian Section Spring Technical Meeting, 2010.

[27] *Characterizing the cyclic variability of ignition timing in a homogeneous charge compression ignition engine fuelled with n-heptane/iso-octane blend fuels.* **M. Shahbakhti, C. Koch.** s.l. : International Journal of Engine Research, 2008, Vol. 9, pp. 361-397.

[28] *Managing SI/HCCI dual-mode engine operation.* **H. Santoso, J. Matthews, W. Cheng.** 2005-01-0162, s.l. : SAE International, 2005.

[29] *Comparison of DME HCCI operating ranges for the thermal stratification and fuel stratification based on a multi-zone model.* **D. Jung, O. Kwon, O. Lim.** 6, s.l. : Journal of Mechanical Science and Technology, 2011, Vol. 25, pp. 1383-1390.

[30] *A review of experimental and simulation studies on controlled auto-ignition combustion.* **N. Milovanovic, R. Chen.** 2001-01-1890, s.l. : SAE International, 2001.

[31] *Comparison of butanol/n-heptane to PRF blended fuels in HCCI engines.* **K. Ebrahimi, M. Shahbakhti, C. Koch.** Winnipeg : Proceedings of Combustion Institute - Canadian Section, 2011.

[32] **Audet, A.** *Closed loop control of HCCI using camshaft phasing and dual fuels.* Edmonton, Alberta : University of Alberta, 2008.

[33] *Thermal and chemical effects of NVO fuel injection on HCCI combustion.* **R. Fitzgerald, R. Steeper.** 2010-01-0164, s.l. : SAE International, 2010.

[34] **Aroonsrisopon, T.** *Analysis of stratified charge operation and negative calve overlap operatin using direct fuel injection in homogeneous charge compression ignition engines.* Madison, Wisconsin : University of Wisconsin-Madison, 2006.

[35] *Effects of negative valve overlap on the auto-ignition process of lean ethanol/air mixture in HCCI-engines.* **T. Joelsson, R. Yu, J. Sjoholm, P. Tunestal, XS. Bai.** 2010-01-2235, s.l. : SAE International, 2010.

[36] **Heywood, J.** *Internal Combustion Engine Fundamentals.* New York : McGraw-Hill, 1988.

[37] **F. Zhao, T. Asmus, D. Assanis, J. Dec, J. Eng, P. Najt.** *Homogeneous Charge Compression Ignition (HCC) Engines: Key Research and Development Issues.* Warrendale PA, USA : SAE International, 2003.

[38] **Kuo, K.** *Principles of Combustion.* Hoboken, New Jersey : John Wiley & Sons, 2005.

[39] *HCCI in a CFR engine: Experiments and detailed kinetic modeling.* **D. Flowers, S. Aceves, R. Smith, J. Torres, J. Girard, R. Dibble.** 2000-01-0328, s.l. : SAE International, 2000.

[40] *Supercharged homogeneous charge compression ignition.* **M. Christensen, B. Johansson, P. Amneus, F. Mauss.** 980787, s.l. : SAE International, 1998.

[41] *A four-stroke homogeneous charge comrpession ignition engine simulation for combustion and performance studies.* **S. Fiveland, D. Assanis.** 2000-01-0332, s.l. : SAE International, 2000.

[42] *An interactively coupled CFD-multi-zone approach to model HCCI combustion.* **C. Felsch, R. Dahms, B. Glodde, S. Vogel, S. Jerzembeck, N. Peters, H. Barths, T. Sloane, N. Wermuth, A. Lippert.** s.l. : Flow Turbulence and Combustion, 2009, Vol. 82, pp. 621-641.

[43] *A six-zone simulation model for HCCI engines with a non-segregated solver of zone state.* **D. Kozarac, Z. Lulic, G. Sagi.** 3, s.l. : Combustion Theory and Modelling, 2010, Vol. 14, pp. 425-451.

[44] *Prediction of carbon monoxide and hydrocarbon emissions in iso-octane HCCI engine combustion using multizone simulations.* **D. Flowers, S. Aceves, J. Martinez-Frias, R. Dibble.** s.l. : Proceedings of the Combustion Institute, 2002, Vol. 29, pp. 687-694.

[45] *Investigating the importance of mass transfer in the formation of HCCI engine emissions using a multi-zone model.* **Komninos, N.** s.l. : Applied Energy, 2009, Vol. 86, pp. 1335-1343.

[46] *Modeling HCCI combustion: Modification of a multi-zone model and comparison to experimental results at varying boost pressure.* **Komninos, N.** s.l. : Applied Energy, 2009, Vol. 86, pp. 2141-2151.

[47] *Multi-dimensional simulation of HCCI engine using parallel computation and chemical kinetics.* **Z. Wang, S-J. Shuai, J-X. Wang.** 2008-01-0966, s.l. : SAE International, 2008.

[48] *Experimental and numerical study of methanol/dimethyl ether dual-fuel compound combustion.* **Z. Chen, M. Yao, Z. Zheng, Q. Zhang.** s.l. : Energy & Fuels, 2009, Vol. 23, pp. 2719-2730.

[49] *A computational study of an HCCI engine with direct injection during gas exchange.* **H. Su, A. Vikhansky, S. Mosbach, M. Kraft, A. Bhave, K.-O. Kim, T. Kobayashi, F. Mauss.** s.l. : Combustion and Flame, 2006, pp. 118-132.

[50] **Tuner, M.** *Stochastic reactor models for engine simulations.* Lund, Sweden : Lund University, 2008.

[51] *Modeling and investigation of exothermic centers in HCCI combustion.* **M. Turner, F. Mauss.** 2009-01-0131, s.l. : SAE International, 2009.

[52] *Gasoline HCCI modeling: Computer program combining detailed chemistry and gas exchange processes.* **R. Ogink, V. Golovitchev.** 2001-01-3614, s.l. : SAE International, 2001.

[53] *Studying the influence of direct injection on PCCI combustion and emissions at engine idle condition using two dimensional CFD and stochastic reactor model.* **L. Cao, H. Su, S. Mosbach, M. Kraft.** 2008-01-0021, s.l. : SAE International, 2008.

[54] *Real-time evaluaton of a detailed chemistry HCCI engine model using a tabulation technique.* **S. Mosbach, A. Aldawood, M. Kraft.** s.l. : Combustion Science and Technology, 2008, Vol. 180, pp. 1263-1277.

[55] *A detailed chemistry simulation of the SI-HCCI transition.* **J. Etheridge, S. Mosbach, M. Kraft, H. Wu.** 2010-01-0574, s.l. : SAE International, 2010.

[56] *A detailed chemistry multi-cycle simulation of a gasonline fuelled HCCI engine operated with NVO.* **J. Etheridge, S. Mosbach, M. Kraft, H. Wu, N. Collings.** 2009-01-0130, s.l. : SAE International, 2009.

[57] *A new heat release rate (HRR) law for homogeneous charge compression ignition (HCCI) combustion mode.* **M. Garcia, F. Aguilar, T. Lencero, J. Villanueva.** s.l. : Applied Thermal Engineering, 2009, Vol. 29, pp. 3654-3662.

[58] *New heat transfer correlation for an HCCI engine derived from measurements of instantaneous surface heat flux.* **J. Chang, O. Guralp, Z. Filipi, D. Assanis, T-W. Kuo, P. Najt, R. Rask.** 2004-01-2996, s.l. : SAE International, 2004.

[59] *A reduced chemical kinetic model for HCCI combustion of primary reference fuels in a rapid compression machine.* **S. Tanaka, F. Ayala, J. Keck.** 4, s.l. : Combustion and Flame, 2003, Vol. 133, pp. 467-481.

[60] *Validity of the single-processor approach to achieving large scale computing capabilities.* **Amdahl, G.** s.l. : Proceedings of AFIPS Conference, 1967.

[61] *Reevaluating Amdahl's law in the multicore era.* **X. Sun, Y. Chen.** s.l. : Journal of Parallel and Distributed Computing, 2010, Vol. 70, pp. 183-188.

[62] *Biomass derived producer gas as a reciprocating engine fuel - an experimental analysis.* **G. Sridhar, P. Paul, H. Mukunda.** s.l. : Biomass & Energy, 2001, Vol. 21, pp. 61-72.

[63] *Hydrocarbon emission from combustion of mixtures of natural gas and hydrogen containing producer gas in a SI engine.* **T. Jensen, J. Schramm, K. Narusawa, and S. Hori.** 2001-01-3532, s.l. : SAE International, 2001.

[64] **Y. Cengel, M. Boles.** *Thermodynamics, An Engineering Approach.* New York : McGraw-Hill, 2006.

[65] *Analysis of design of pure ethanol engines.* **Boretti, A.** 2010-01-1453, s.l. : SAE International, 2010.

[66] *Kinetics modeling of shock-induced ignition in low-dilution CH4/O2 mixtures at high pressures and intermediate temperatures.* **E. Petersen, D. Davidson, R. Hanson.** s.l. : Combustion and Flame, 1999, Vol. 117, pp. 272-290.

[67] *A comprehensive modeling study of methane oxidation.* **H. Curran, S. Gallagher, J. Simmie.**

[68] **Curran, H.** Detailed chemical kinetic modeling; Is there life after GRI-MECH 3.0?

[69] *Methane/propane oxidation at high pressures: Experimental and detailed chemical kinetic modeling.* **E. Petersen, D. Kalitan, S. Simmons, G. Bourque, H. Curran, J. Simmie.** s.l. : Proceedings of the Combustion Institute, 2007, Vol. 31, pp. 447-454.

[70] G. Smith, D. Golden, M. Frenklach, N. Moriarty, B. Eiteneer, M. Goldenberg, C. Bowman, R. Hanson, S. Song, W. Gardiner, Jr., V. Lissianski, Z. Qin. [Online] http://www.me.berkeley.edu/gri_mec.

[71] *Development and testing of a comprehensive chemical mechanism for the oxidation of methane.* **K. Hughes, T. Turanyi, A. Clague, M. Pilling.** 9, s.l. : International Journal of Chemical Kinetics, 2001, Vol. 33, pp. 513-538.

[72] The Leeds methane oxidation mechanism. [Online] http://www.chem.leeds.ac.uk/combustion/methane.htm.

[73] *Development and validation of a detailed reaction mechanism for the combustion of small hydrocarbons.* **Konnov, A.** Edinburgh : 28th International Symposium on Combustion, 2000.

[74] *Modeling of non-catalytic partial oxidation of natural gas under conditions found in industrial reformers.* **Xinwen Zhou, Caixia Chen, Fuchen Wang.** 1, s.l. : Chemical Engineering and Processing: Process Intensification, 2010, Vol. 49, pp. 59-64.

[75] *Development of a natural gas reaction mechanism for engine simulations based on rapid compression machine experiments using a multi-objective optimisation strategy.* **S. Heyne, A. Roubaud, M. Ribaucour, G. Vanhove, R. Minetti, D. Favrat.** s.l. : Fuel, 2008, Vol. 87, pp. 3046-3054.

[76] *Prechamber auto-ignition.* **Heyne, S.** Dubendorf : Low Carbon Fuels - EMPA, 2005.

[77] *Kinetics simulations of high pressure CH4-O2 mixtures.* **R. Pellegrini, C. Bruno, E. Giacomazzi.** Huntsville, Alabama : 39th AIAA/ASME/SAE/ASEE Joint Propulsion Conference & Exhibit, 2003.

[78] *Ignition properties of methane/hydrogen mixtures in a rapid compression machine.* **S. Gersen, N. Anikin, A. Mokhov, H. Levinsky.** s.l. : International Journal of Hydrogen Energy, 2008, Vol. 33, pp. 1957-1964.

[79] *Understanding of controlled autoignition combustion in a four-stroke gasoline engine.* **H. Zhao, Z. Peng, N. Ladommatos.** s.l. : Proceedings of the Institution of Mechanical Engineers Part D, 2001, Vol. 215, pp. 1297-1310.

[80] *Combustion timing in HCCI engines determined by ion-sensor: Experimental and kientic modeling.* **P. Mehresh, J. Souder, D. Flowers, U. Riedel, R. Dibble.** s.l. : Proceedings of the Combustion Institute, 2005, Vol. 30, pp. 2701-2709.

[81] *Fuel effects on NOx emissions in partially premixed flames.* **S. Naha, S. Aggarwal.** s.l. : Combustion and Flame, 2004, Vol. 139, pp. 90-105.

[82] *Scalar profiles and NO formation in laminar opposed-flow partially premixed methane/air flames.* **R. Barlow, A. Karpetis, J. Frank, J-Y. Chen.** s.l. : Combustion and Flame, 2001, Vol. 127, pp. 2102-2118.

[83] *Simulation of NOx formation in dilute H2/CO/N2-air diffusion flames using full and reduced kinetics.* **W. Collins, S. Hochgreb, N. Swaminathan, J-Y. Chen.** Cambridge : Third European Combustion Meeting, 2007.

[84] *Combustion of n-butanol in a spark-ignition IC engine.* **S. Szwaja, J. Naber.** s.l. : Fuel, 2010, Vol. 89, pp. 1573-1582.

[85] *Developments in biobutanol production: New insights.* **M. Kumar, K. Gayen.** s.l. : Applied Energy, 2011, Vol. 88, pp. 1999-2012.

[86] *Experimental and modeling study of the kinetics of oxidation of butanol-n-heptane mixtures in a jet-stirred reactor.* **P. Dagaut, C. Togbe.** s.l. : Energy & Fuels, 2009, Vol. 23, pp. 3527-3535.

[87] *Biobutanol - Production and Purfication Methods.* **W. Kaminski, E. Tomczak, A. Gorak.** Uroczysko, Poland : 19th Central European Conference ECOpole, 2010.

[88] *Bio-butanol: Combustion properties and detailed chemical kinetic model.* **G. Black, H.Curran, S. Pichon, J.Simmie, V. Zhukov.** s.l. : Combustion and Flame, 2010, Vol. 157, pp. 363-373.

[89] *A comprehensive modeling study of n-heptane oxidation.* **H. Curran, P. Gaffuri, W. Pitz, C. Westbrook.** s.l. : Combustion and Flame, 1998, Vol. 114, pp. 149-177.

[90] *Extinction and autoignition of n-heptane in counterflow configuration.* **R. Seiser, H. Pitsch, K. Seshadri, W. Pitz, H. Curran.** s.l. : Proceedings of the Combustion Institute, 2000, Vol. 28, pp. 2029-2037.

[91] *A comprehensive modeling study of iso-octane oxidation.* **H. Curran, P. Gaffuri, W. Pitz, C. Westbrook.** s.l. : Combustion and Flame, 2002, Vol. 129, pp. 253-280.

[92] **C. Bowman, R. Hanson, D. Davidson, W.Gardiner, Jr., V. Lissianski, G. Smith, D. Golden, M. Frenklach, M. Goldenberg.** [Online] http://www.me.berkeley.edu/gri_mech/.

[93] *Numerical study of a HCCI engine fuelled with biogas.* **S. Visakhamoorthy, T. Tzanetakis, D. Haggith, A. Sobiesiak, J. Wen.** s.l. : Applied Energy - under review, 2011.

[94] **Glassman, I.** *Combustion.* San Diego : Academic Press, 1996.

Appendix A: Changing the Fuel

The majority of the adjustable parameters in this model are available through the input.txt file. Through this file, many parameters can be adjusted such as engine operating conditions, array sizes, and timestep adjustments. However, due to the way the model is structured, changing the fuel or the chemical mechanism of the fuel requires changing the code itself and requires some understanding of how the model works. To change the fuel type used in this model, the steps below will need to be performed. For just changing the chemical mechanism, steps 2 to 8 can be omitted. However, implementing these changes in the model is best done after some understanding of the initial model specification is gained.

1. A chemical input file containing all reaction data must be created. This file, chem.asc, is created by using the thermodynamic data file (therm.dat) and the reaction mechanism file. Running both these files as inputs for GPCK.exe will allow the GPCK.exe preprocessor to create the chem.asc file. This file is then placed in the operating folder of the simulation and included during compilation of the model. When running the GPCK.exe preprocessor, any inconsistencies in the mechanism or thermodynamic files (such as inconsistent letter case) will be detected as errors.
    a. If creating a chemical mechanism file from multiple mechanisms, ensure that all text is either upper case or lower case, not a combination of both
    b. If multiple mechanisms are combined, the therm.dat file must contain reaction data for all species contained in the final reaction mechanism
    c. Place both mechanism and thermodynamic data files in the same folder as GPCK.exe before executing

2. Establish method of setting fuel mixture ratio (assuming fuel comprises multiple components that will be varied – ie biogas study or butanol/n-heptane study)
    a. Can be specified entirely through the input file (in the case of biogas – test_v6 folder)
        i. Molar fractions of the fuel constituents are already known from the experimental data
    b. Can have the model calculate molar fuel ratios using volumetric ratio inputs (in the case of butanol/n-heptane – test_v7 folder)
        i. Molar fractions are unknown and need to be calculated. For example, liquid fuels are often specified by volume, so the molar fractions will need to be determined. This conversion can get tedious to do every time the fuel ratio is changed so it can be hard coded into the model such that volumetric inputs can still be used.
3. Calculate a general form balanced stoichiometric equation of the fuel air mixture combustion. For this step and the following, all examples will be based on the butanol/n-heptane work.
    a. Assumptions:
        i. air = 79% N_2 and 21% O_2
        ii. Complete combustion in excess air → reaction products consist of CO_2, H_2O, and N_2
    b. Example:

        a = mole fraction of butanol

        b = mole fraction of n-heptane

where a + b = 1.0 as the equation being calculated is for one mol of fuel reacted in a stoichiometric volume of air and the ratio is known based on the volumetric ratios of the two fuels:

$[aC_4H_{10}O + bC_7H_{16}] + n_{air}[0.79N_2 + 0.21O_2] \rightarrow (4a + 7b)CO_2 + (5a + 8b)H_2O + (0.79n_{air})N_2$ where through balancing the reaction, $n_{air} = (12a+22b)/0.42$

4. Update the equation for calculating stoichiometric combustion. Example:

   AFSTOICH=((12*a)+(22*b))/0.42

   MWFUEL = (a*MW_BUT)+(b*MW_NHP)

   AFSTOICH=(AFSTOICH*MWAIR)/(1*MWFUEL)

   OXYGEN=RLAMBDA*AFSTOICH

   OXYGEN=OXYGEN*1*MWFUEL

   OXYGEN=OXYGEN/MWAIR

5. Enter the stoichiometric molar fractions into the model under the ZNXX variables, where XX is the species. These ZNXX variables then act as temporary values. Example:

   ZNCO2=(4*a)+(7*b)

   ZNH2O=(5*a)+(8*b)

   ZNN2=0.79*OXYGEN

   ZNO2=(0.21*OXYGEN)-(6*a)-(11*b)

6. Calculate a general form balanced excess air reaction of the fuel in excess air.

   a. Assumptions: same as step 3

   b. $[aC_4H_{10}O + bC_7H_{16}] + n_{air,\ excess}[0.79N_2 + 0.21O_2] \rightarrow (4a + 7b)CO_2 + (5a + 8b)H_2O + (0.79n_{air,\ excess})N_2 + (0.21n_{air,\ excess} - 6a - 11b)O_2$

where $n_{air,\ excess}$ is a known quantity from the equivalence ratio and the moles of O_2 in the reactants is found through balancing.

7. Now molar ratios of reactants and products are known in a balanced excess air situation. However, the complete intake charge also consists of burned gases which come from trapped residuals and EGR.
    a. Assumptions:
        i. Trapped and recycled gases consist only of completely burned reactants
        ii. These gases are the same temperature as the intake charge – which is not true in the experimental case, especially during negative valve overlap
    b. Fraction of charge in the combustion chamber that is composed of only burned reactants is given by: $x_b=(EGR\%/100)(1 - x_r) + x_r$ where x_r is fraction of trapped residuals and EGR is in %. Using this, the overall composition of the combustion chamber can be specified.
    c. Continuing the above example:

        $(1-x_b)\{[aC_4H_{10}O + bC_7H_{16}] + n_{air,\ excess}[0.79N_2 + 0.21O_2]\} + x_b\{(4a + 7b)CO_2 + (5a+8b)H_2O + (0.79n_{air,\ excess})N_2 + (0.21n_{air,\ excess} – 6a – 11b)O_2\}$

        Simplifying this results in an overall charge composition of:

        $(1-x_b)aC_4H_{10}O + (1-x_b)bC_7H_{16} + x_b(4a + 7b)CO_2 + x_b(5a + 8b)H_2O + 0.79n_{air,\ excess}N_2 + (0.21n_{air,\ excess} – 6ax_b – 11bx_b)O_2$

8. Enter the excess air molar fractions into the model under FNXX variables, where XX is the species. The FNXX variables are then passed into the molar fraction species array, XTMP in the next step.

    EGRNUM=EGR/100

XBURNT=EGRNUM*(1-RESFRAC)+RESFRAC

FN_BUT=a*(1-XBURNT)

FN_NHP=b*(1-XBURNT)

FNN2=ZNN2

FNCO2=XBURNT*ZNCO2

FNO2=(0.21*OXYGEN)-(6*a*XBURNT)-(11*b*XBURNT)

FNH2O=XBURNT*ZNH2O

TOTMOL=FN_BUT+FN_NHP+FNN2+FNCO2+FNO2+FNH2O

9. In addition to setting the mole fraction values to each species variable in the intake charge, the species variables need to be allocated to their proper array locations in XTMP. These array locations will vary with the chemical mechanism used and need to be updated whenever the fuel is changed. Continuing the example:
    a. Array locations in XTMP match the locations of species in the chem.asc data file. A section containing only the species in the example mechanism is shown below:

Excerpt containing a section of the species listing from butanol/n-heptane chem.asc.

```
h2          o2          h2o         ch2o        co
co2         ch4         c2h6        c2h4        c2h2
ch3cho      c3h6        nc7h16      c4h9oh      nc3h7cho
c4h6        c4h8-1      c5h10-1     c6h12-1     n2
c4h7ohz     c3h5oh      ac4h8oh     pc4h9o      dc4h8oh
cc4h8oh     c4h8oh-1    cc3h6oh     c3h6oh      c3h6cho-1
```

b. Array locations are counted off from 1 starting at the left most column and working to the right. For example, CO_2 has the 6^{th} location.

c. Using the chem.asc file, array locations for all the species present in the intake charge can be identified and then assigned as shown below:

XTMP(2)=FNO2

XTMP(3)=FNH2O

XTMP(6)=FNCO2

XTMP(13)=FN_NHP

XTMP(14)=FN_BUT

XTMP(20)=FNN2

10. Variables in the input file need to be updated. These include engine, timestep, and array length parameters. Appendix C outlines a list of variables that may need to be changed. Additionally, memory stack size may need to be increased depending on the size of the chemical mechanism being used. This can be adjusted in ProFortran itself – under Project Options → Linker → Additional Options. Enter "-stack:XX" where "XX" is the stack size. See figure below.

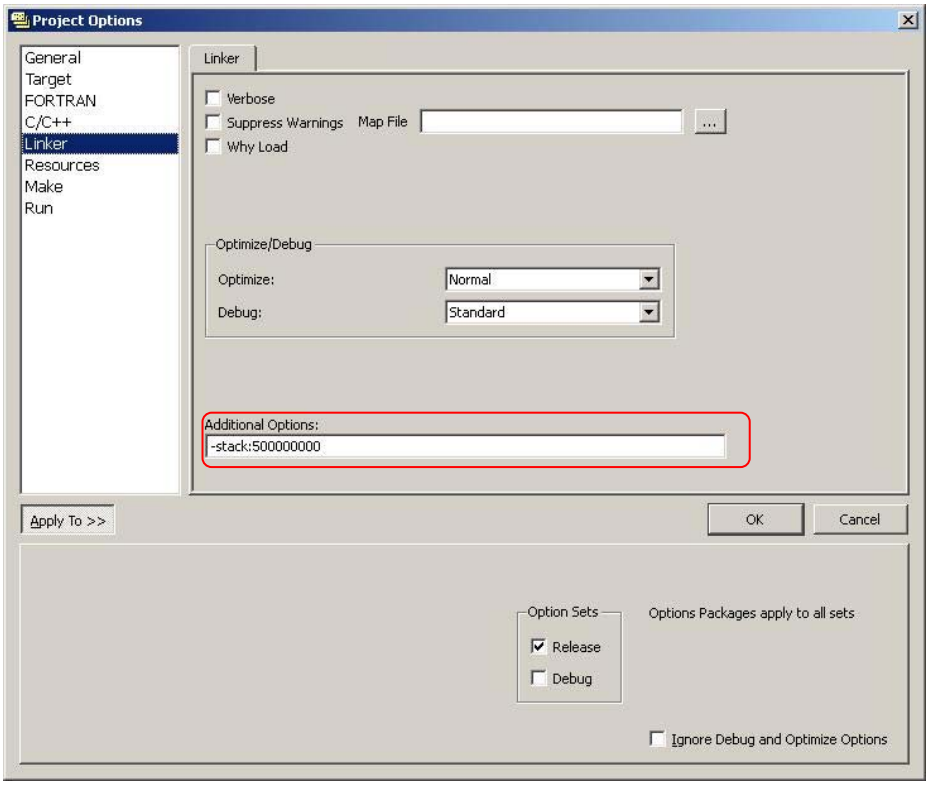

11. Finally, changes will need to be made to the code used to write the output file headers as large chemical mechanisms may overflow onto subsequent lines instead of writing everything into one line.
    a. In the file CONV.F, label 200 needs to be edited such that the format is (# of species + 14). For example, from the butanol/n-heptane work, the number of species in the mechanism used was 200.
        i. 200 FORMAT(F25.8,**214**(',',F25.8))
    b. Similarly, in CONV_DRIVER.F90, label 120 needs to be edited such that the format is also (# of species + 14). Once again, from the butanol/n-heptane example, the number of species is 200 resulting in a format value of 214.
        i. 120 FORMAT (A,A,A,**214**(',',A))

Appendix B: Adjusting Temporal Resolution

When the engine being modeled is changed, engine speed is changed, or when temporal resolution needs to be increased, the timestep parameters of the model need to be adjusted to maintain the required resolution. The actual temporal resolution in the model is defined by DTHETA which is the incremental crank angle that the simulation steps through as it iterates through the closed cycle period of the engine. The smaller DTHETA is, the more increments the crank angle range is sliced into. DTHETA is a function of DT and SPEED (DTHETA = 6*SPEED*DT as defined in the code itself).

When the engine speed is changed and the user wishes to maintain a constant DTHETA, DT will need to be adjusted to account for this. Similarly, if the temporal resolution needs to be increased or decreased, an adjustment of DT is necessary as engine speed is fixed.

However, if the overall engine is changed, as is the case usually when simulating a new set of experimental data, it is likely that the timing of IVC and EVO is different. This will change the overall range that the model operates through. To address this, TFIN will need to be calculated. TFIN is the time, in seconds, it takes the engine to operate from IVC to EVO and depends on the valve timing and engine speed. Following this, a DTHETA will need to be selected and from here, DT can be found. For example, given a valve timing of IVC at 159˚ bTDC and EVO at 80˚ aTDC and an engine speed of 1021RPM, as in the case of the butanol/n-heptane work:

$$TFIN = \frac{159^\circ + 80^\circ}{1021RPM * 360^\circ/60sec}$$

$$TFIN = 0.039sec$$

Assuming a DTHETA of 0.042 is sufficient:

$$DTHETA = 6 * SPEED * DT$$

$$DT = \frac{DTHETA}{6 * SPEED}$$

$$DT = \frac{0.042^{\circ}}{6\frac{^{\circ} \cdot min}{rev \cdot sec} * 1021RPM}$$

$$DT = 6.856 * 10^{-6} sec$$

Appendix C: List of Parameters

LENIWK	Integer work array length – change when chemical mechanism is changed
LENRWK	Real work array length – change when chemical mechanism is changed
LENCWK	Character work array – change when chemical mechanism is changed
KMAX	Length of species array – set to (# of species + 1) – varies with chemical mechanism
KSAVER	Length of ODE common block
COMPR	Compression ratio
RATIO	Ratio of connection rod length to crank arm radius
BORE	Cylinder bore diameter (cm)
STROKE	Engine stroke length (cm)
CADINI	Initial engine crank angle (degrees) – crank angle at IVC, when the model start
SPEED	Engine speed (RPM)
TWALL	Wall temperature (°C) – unless directly measured, usually set to 20 degrees warmer than coolant temperature
C1	Woschni heat transfer coefficient 1
C2	Woschni heat transfer coefficient 2
CBB	Blow-by constant
COREPCT	Fraction of cylinder volume in core zone
GEOMR	Geometric ratio – rate at which zones get successively smaller as one approaches the cylinder wall
MWAIR	Molecular weight of air (g/mol)
PHI	Equivalence ratio (fuel/air ratio)
EGR	Percent exhaust gas recirculation (%)
RESFRAC	Fraction of trapped residual gas
PINTAKE	Cylinder pressure at IVC (atm)
TINTAKE	In-cylinder temperature at IVC (K)
HTCFAC	Heat transfer scaling factor applied to Woschni correlation
ZERO	Reference 0.0 value
PI	Reference PI value
NDEG	Degree of polynomial solved by ZPORC
RTOL	Relative tolerance for solution values (see DVODE)
ATOL	Absolute tolerance for solution values (see DVODE)
DT	Time step (s)
TFIN	For a given engine speed and valve timing, time from IVC to EVO (s)
LSCREN	Output flag
LINCK	Linking file
LINTR	Linking file
LOUT	Main output file
TWIDTH	Temperature difference between outermost and core zone. + = cold core, - = hot core
NZONES	# of zones in simulation

Appendix D: Graphical Representation of Numerical Algorithm

The algorithm followed by the numerical simulation and a brief explanation of the equations is presented in the background section of this report. However, for the sake of clarity, an alternative representation of the numerical algorithm is shown below. It outlines a general case situation to give the reader a better idea of how the model works. Each individual picture represents the state of the cylinder after a specific step in the numerical algorithm.

The alternative graphical representation begins after the initial conditions and zone allocation steps are complete. It starts at constant volume zone combustion and ends at the final pressure equalization. This inner loop of the algorithm is done for each incremental crank angle that the simulation steps through from IVC to EVO. When the incremental crank angle has stepped to the EVO crank angle, the model terminates. Subscripts on pressure and temperature refer to specific zones (1 being the core). Superscripts on these two properties refer to a change - for example, if the pressure of zone 1 increase, it changes from P_1^1 to P_1^2. Subscripts on volume simply indicate whether a new overall volume has been calculated - they do not refer to zones.

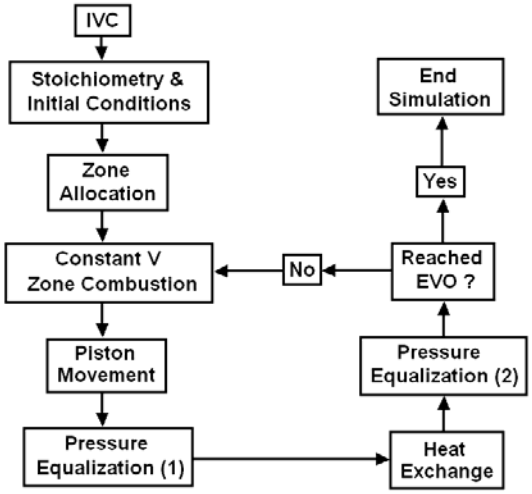
IVC
Stoichiometry & Initial Conditions
Zone Allocation
Constant V Zone Combustion
Piston Movement
Pressure Equalization (1)
Heat Exchange
Pressure Equalization (2)
Reached EVO ?
No
Yes
End Simulation

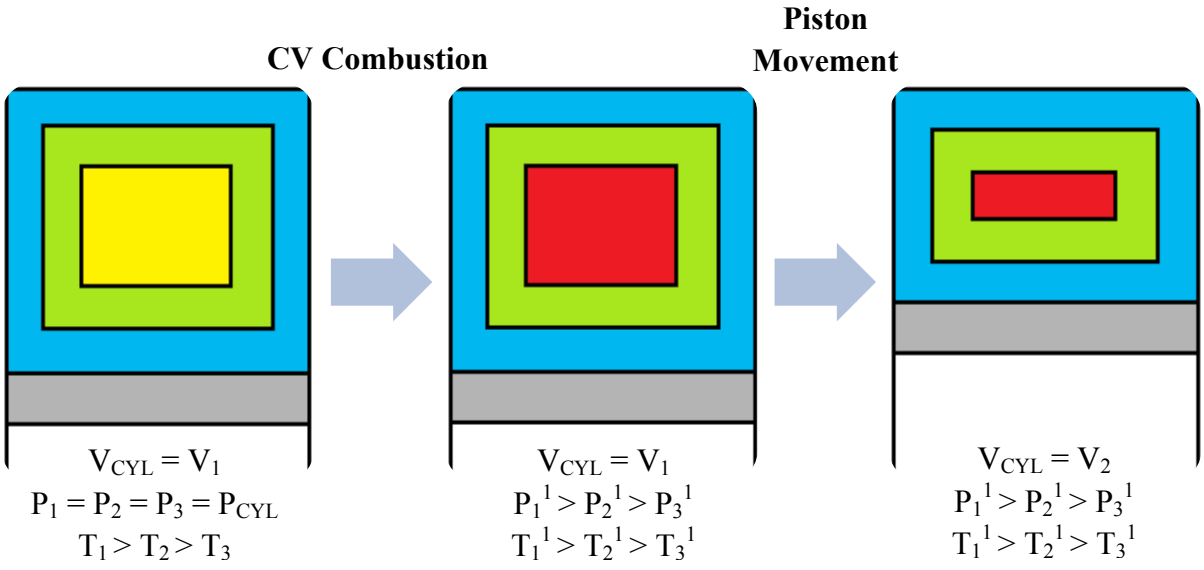
CV Combustion
Piston Movement
$V_{CYL} = V_1$
$P_1 = P_2 = P_3 = P_{CYL}$
$T_1 > T_2 > T_3$
$V_{CYL} = V_1$
$P_1^1 > P_2^1 > P_3^1$
$T_1^1 > T_2^1 > T_3^1$
$V_{CYL} = V_2$
$P_1^1 > P_2^1 > P_3^1$
$T_1^1 > T_2^1 > T_3^1$

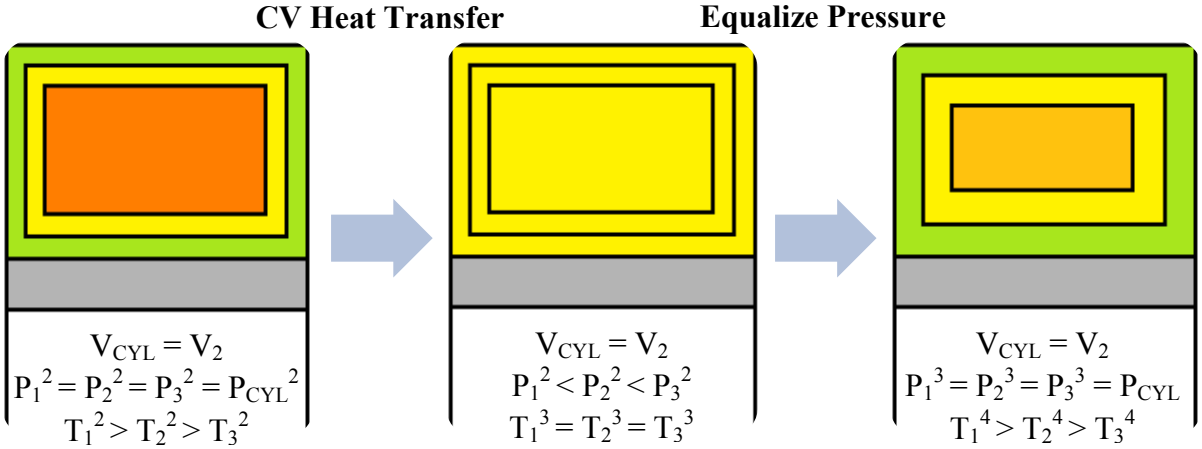
CV Heat Transfer
Equalize Pressure
$V_{CYL} = V_2$
$P_1^2 = P_2^2 = P_3^2 = P_{CYL}^2$
$T_1^2 > T_2^2 > T_3^2$
$V_{CYL} = V_2$
$P_1^2 < P_2^2 < P_3^2$
$T_1^3 = T_2^3 = T_3^3$
$V_{CYL} = V_2$
$P_1^3 = P_2^3 = P_3^3 = P_{CYL}$
$T_1^4 > T_2^4 > T_3^4$